Changes in active-site geometry on X-ray photoreduction of a lytic polysaccharide monooxygenase active-site copper and saccharide binding

Tobias Tandrup, Sebastian J. Muderspach, Sanchari Banerjee, Gianluca Santoni, Johan Ø. Ipsen, Cristina Hernández-Rollán, Morten H. H. Nørholm, Katja S. Johansen, Flora Meilleur and Leila Lo Leggio

Changes in active-site geometry on X-ray photo-reduction of a lytic polysaccharide monooxygenase active-site copper and saccharide binding

Tobias Tandrup,[a] Sebastian J. Muderspach,[a] Sanchari Banerjee,[a] Gianluca Santoni,[b] Johan Ø. Ipsen,[c] Cristina Hernández-Rollán,[d] Morten H. H. Nørholm,[d] Katja S. Johansen,[c] Flora Meilleur[e,f] and Leila Lo Leggio[a]*

[a]Department of Chemistry, University of Copenhagen, Universitetsparken 5, 2100-DK, Copenhagen, Denmark, [b]ESRF, Structural Biology Group, 71 avenue des Martyrs, 38027 Grenoble cedex, France, [c]Department of Geosciences and Natural Resource Management, University of Copenhagen, 1958-DK, Frederiksberg, Denmark, [d]Novo Nordisk Foundation Center for Biosustainability, Technical University of Denmark, 2800-DK, Kgs. Lyngby, Denmark, [e]Department of Molecular and Structural Biochemistry, North Carolina State University, Campus Box 7622, Raleigh, NC 27695, USA, and [f]Neutron Scattering Division, Oak Ridge National Laboratory, PO Box 2008, Oak Ridge, TN 37831, USA. *Correspondence e-mail: leila@chem.ku.dk

The recently discovered lytic polysaccharide monooxygenases (LPMOs) are Cu-containing enzymes capable of degrading polysaccharide substrates oxidatively. The generally accepted first step in the LPMO reaction is the reduction of the active-site metal ion from Cu^{2+} to Cu^+. Here we have used a systematic diffraction data collection method to monitor structural changes in two AA9 LPMOs, one from *Lentinus similis* (*Ls*AA9_A) and one from *Thermoascus aurantiacus* (*Ta*AA9_A), as the active-site Cu is photoreduced in the X-ray beam. For *Ls*AA9_A, the protein produced in two different recombinant systems was crystallized to probe the effect of post-translational modifications and different crystallization conditions on the active site and metal photoreduction. We can recommend that crystallographic studies of AA9 LPMOs wishing to address the Cu^{2+} form use a total X-ray dose below 3×10^4 Gy, while the Cu^+ form can be attained using 1×10^6 Gy. In all cases, we observe the transition from a hexacoordinated Cu site with two solvent-facing ligands to a T-shaped geometry with no exogenous ligands, and a clear increase of the θ_2 parameter and a decrease of the θ_3 parameter by averages of 9.2° and 8.4°, respectively, but also a slight increase in θ_T. Thus, the θ_2 and θ_3 parameters are helpful diagnostics for the oxidation state of the metal in a His-brace protein. On binding of cello-oligosaccharides to *Ls*AA9_A, regardless of the production source, the θ_T parameter increases, making the Cu site less planar, while the active-site Tyr—Cu distance decreases reproducibly for the Cu^{2+} form. Thus, the θ_T increase found on copper reduction may bring *Ls*AA9_A closer to an oligosaccharide-bound state and contribute to the observed higher affinity of reduced *Ls*AA9_A for cellulosic substrates.
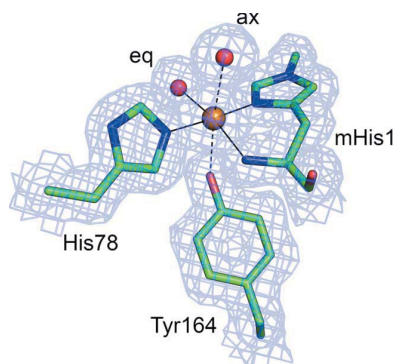
1. Introduction

25–50% of all proteins contain metal cofactors (metalloproteins) (Hoppert, 2011; Waldron *et al.*, 2009) and govern a range of biological functions, such as non-enzymatic electron charge transfer, metal transport and storage (Hoppert, 2011), and catalysis (Chen *et al.*, 2019). Redox activities, specifically, are often associated with enzymes containing iron and copper (Hoppert, 2011; Bowman *et al.*, 2016). Protein Cu centres are involved in metal transport, regulation and oxidation of various compounds (Festa & Thiele, 2011), and are often defined by the number and character of ligands coordinating the metal (Solomon *et al.*, 2014).

electronic reprint

In X-ray crystallography experiments, crystals of metalloproteins absorb energies in the X-ray range more readily than a de-metallized form of the protein due to the presence of the transition metals (Handing *et al.*, 2018). Metalloproteins are therefore more predisposed to radiation damage than proteins not containing metals. With the increase in flux and intensity of X-rays at the new synchrotron beamlines, X-ray studies on metalloproteins become more challenging. It is estimated that only 10% of the interacting X-ray photons are scattered by crystals during data collection (Bowman *et al.*, 2016). The interacting but non-scattering photons may be absorbed and result in either heat increase or radiation damage (Helliwell, 1984). Photoreduction is therefore commonly observed in the structures of metalloproteins determined by X-rays. Metal centres may be found to change electronically and structurally (Bowman *et al.*, 2016), as can be monitored by spectroscopy and/or shown by increasing bond distances and altered bond angles between the metal and its ligands (Bowman *et al.*, 2016; Frankaer *et al.*, 2014; Corbett *et al.*, 2007; Antonyuk & Hough, 2011; Yano *et al.*, 2005). Such distorted metal coordination geometry may lead to the incorrect identification of the metal ion and the catalytic mechanism, especially of a redox protein.

When performing a diffraction experiment, the incoming photons of the X-ray beam may reduce the metal of metalloproteins even at low doses. This makes the structure determination of the native/resting state difficult. One way of circumventing photoreduction is to use neutrons instead of X-rays for crystallographic studies of metalloproteins (Schröder & Meilleur, 2021), though this imposes severe limitations on the systems that can be studied, as much bigger crystals are required for neutron diffraction. Furthermore, reduction of transition metals by X-rays may be a convenient reaction trigger for studies of enzymatic reactions in crystals (Bourgeois & Weik, 2009; Bourgeois & Royant, 2005). Two strategies used to study reaction intermediates structurally are either a real-time approach (serial crystallography) or a trapping approach (conventional crystallography) (Bourgeois, 2017; Schotte *et al.*, 2012).

Lytic polysaccharide monooxygenases [LPMOs, reviewed in Tandrup *et al.* (2018), Vu & Ngo (2018), Wang *et al.* (2020) and Eijsink *et al.* (2019)] were discovered just over 10 years ago and are metalloenzymes containing a type II Cu centre (Quinlan *et al.*, 2011). A Cu^{2+} ion is coordinated by two histidines in a motif known as the histidine brace (His-brace), where the N-terminal His is often $N^{\varepsilon 2}$-methylated in LPMOs of fungal origin and coordinates Cu using both the N-terminal nitrogen and the $N^{\delta 1}$ atom (see Fig. 1) (Quinlan *et al.*, 2011). The His-brace motif is also found in other non-LPMO copper proteins (Labourel *et al.*, 2020; Garcia-Santamarina *et al.*, 2020; Udagedara *et al.*, 2019; Cao *et al.*, 2018). Known LPMOs degrade lignocellulose-, hemicellulose-, chitin-, starch- or pectin-containing biomass oxidatively, and have a boosting effect on saccharification together with glycoside hydrolases (Harris *et al.*, 2010; Lo Leggio *et al.*, 2015; Quinlan *et al.*, 2011; Vaaje-Kolstad *et al.*, 2010; Zerva *et al.*, 2020), thus attracting considerable industrial interest for the production of biofuel (Hemsworth *et al.*, 2013; Müller *et al.*, 2015; Beeson *et al.*, 2015;

Johansen, 2016) and other biotechnological applications (Ipsen *et al.*, 2021). LPMOs are widespread in nature and have been identified in all domains of life, though so far not in mammals. In the CAZy (Carbohydrate-Active enZymes) database, they are classified as Auxiliary Activity families 9–17 (family 12 excluded) (Lombard *et al.*, 2014), with AA17 recently discovered in oomycetes having activity against pectin (Sabbadin *et al.*, 2021).

LPMOs cleave the glycosidic bond, producing both oxidized (C1 and/or C4) and non-oxidized chain ends. Their mechanism (see the simplified LPMO reaction scheme in Fig. 1) has been researched extensively since their discovery. An essential (though probably not rate limiting) step is the reduction of the metal cofactor Cu^{2+} to Cu^{+}, which in nature can be carried by a number of electron donors, such as small molecules or proteins found in their natural environment (Kracher *et al.*, 2016; Várnai *et al.*, 2018; Brenelli *et al.*, 2018; Frommhagen *et al.*, 2017; Wang *et al.*, 2020). *In vitro* reductants such as ascorbic acid, gallic acid or cysteine are commonly used (Wang *et al.*, 2020). As well as being essential for further reactivity, there are several reports indicating increased polysaccharide affinity on reduction of the active-site metal, suggesting that polysaccharide binding precedes further steps in the mechanism (Kracher *et al.*, 2018; Hangasky & Marletta, 2018; Filandr *et al.*, 2020; Brander, Tokin *et al.*, 2021). Both O_2 and H_2O_2 have been suggested as natural co-substrates (Bissaro *et al.*, 2017; Hangasky *et al.*, 2018) and the LPMO mechanism is being assessed continuously for the involvement of either/both (Bissaro *et al.*, 2020; Hedegård & Ryde, 2017; Courtade *et al.*, 2020; McEvoy *et al.*, 2021; Brander *et al.*, 2020). The dependence on H_2O_2 for saccharide cleavage has been established recently specifically for one of the model LPMOs investigated here (Brander, Tokin *et al.*, 2021), and is generally gaining increasing support. The H_2O_2-driven mechanism has the advantage that the LPMO active-site metal only needs to be reduced once, while in the O_2-driven mechanism, it needs to be reduced at every cycle (Bissaro *et al.*, 2017). However, too high levels of H_2O_2 cause oxidative damage and destruction of the enzymes, complicating its use as co-substrate (Müller *et al.*, 2018), and H_2O_2 will react with other chemical species, leading to unwanted decarboxylating reactions in complex substrates, such as lignocellulose, under industrially relevant conditions (Peciulyte *et al.*, 2018).

For LPMOs, X-rays may possibly circumvent the need for additional reducing agents in structural studies of the reaction (Fig. 1). Previously, photoreduction of LPMOs has been studied in detail for members of AA10 and AA13 (Gudmundsson *et al.*, 2014; Muderspach *et al.*, 2019), and somewhat more qualitatively for AA9 (Frandsen *et al.*, 2016).

Here we further investigated the gradual photoreduction of the LPMO active-site Cu^{2+} in a systematic way and monitored the structural changes in two AA9 LPMOs which have been studied extensively. We studied the primarily C4-oxidizing AA9 LPMO from the fungus *Lentinus similis* (*Ls*AA9_A), which is active on soluble cello-oligosaccharides and polysaccharides. We exposed crystals of ligand-free and cello-oligosaccharide-binding *Ls*AA9_A to different radiation

doses. To investigate the effect of post-translational modification and/or crystallization conditions on the metal-centre X-ray-induced perturbation, we carried out a similar study with *Ls*AA9_A produced in *E. coli* [*Ls*AA9_A(*Ec*)], thus devoid of glycosylation and His methylation. We determined a total of six structures *per* substrate-free enzyme and six structures *per* enzyme solved with bound cello-oligosaccharide. Additionally, we have solved six structures of the C1/C4-oxidizing AA9 from *Thermoascus aurantiacus* (*Ta*AA9_A, where oligosaccharides bound in the structure have so far not been obtained) to identify similarities between AA9s as the central Cu ion is reduced. We report how interatomic distances and other geometric parameters within the active site change as a function of the X-ray dose, and as Cu transitions from Cu^{2+} to Cu^+. We have correlated our photoreduced structures to the chemically reduced structure of

*Ls*AA9_A and two structures solved from data collections at room temperature. Furthermore, we have monitored photoreduction in a Serial Synchrotron Crystallography (SSX) experiment of *Ls*AA9_A. The results of the study are relevant both for the general study of metalloproteins by X-ray crystallography and the specific understanding of the LPMO mechanism.

2. Methods

2.1. Crystallization

Crystallization *via* sitting-drop vapour diffusion was performed in MRC two-drop plates set up by an ORYX-8 robot (Douglas Instruments), unless otherwise stated. Cello-oligosaccharides used for substrate-bound structures were purchased from Megazyme.
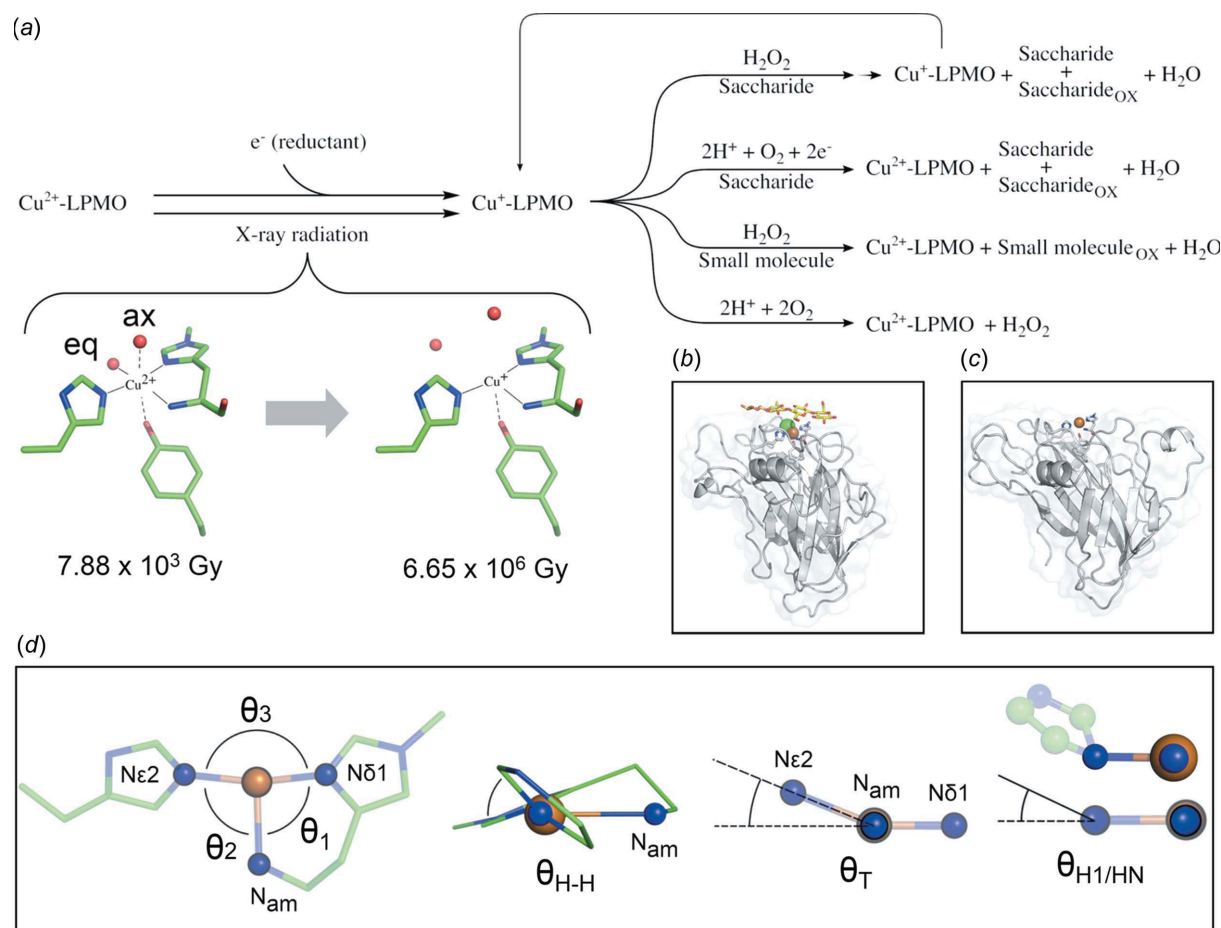

Figure 1
Illustrated is a simplified lytic polysaccharide monooxygenase (LPMO) reaction scheme. (*a*) LPMOs can engage in a variety of reactions depending on the specific enzyme. After Cu reduction, reactions with O_2 and/or H_2O_2 may occur, involving saccharides or a variety of small molecules, in some cases in several steps (Brander, Tokin *et al.*, 2021; Brander, Lausten *et al.*, 2021). Saccharide substrates produce smaller oxidized and/or non-oxidized saccharides as products. The first step in the reaction can be triggered either chemically by a reducing agent or using X-ray photons. The transition from Cu^{2+} to Cu^+ results in expulsion of the equatorial (eq) and axial (ax) ligand water molecules in the type II Cu site. These ligands may be different based on the crystallization liquor components. Upon binding of the substrate, the axial water molecule is displaced. The *Ls*AA9_A His-brace is shown at low (left; PDB entry 7pxi) and high (right; PDB entry 7pxn) X-ray dose (see results). (*b*) The overall structure of *Ls*AA9_A binding cellotetraose (PDB entry 6ydg). (*c*) The overall structure of *Ta*AA9_A (PDB entry 3zud). (*d*) The bond angles referenced throughout the article are defined in Vu & Ngo (2018). Angles θ_1, θ_2 and θ_3 are measured from N—Cu—N as indicated. $\theta_{H–H}$ is the angle between the two His imidazole ring planes. θ_T is the angle between the $N^{\delta 1}$—Cu—N_{am} plane and the $N^{\epsilon 2}$—Cu line. θ_{H1} (also denoted θ_{HN}) is the angle between one His imidazole ring plane and the line from Cu to the Cu-interacting N atom of the same imidazole ring.

The fungal enzyme *Ls*AA9_A was expressed in *A. oryzae* [*Ls*AA9_A(f)], purified and deglycosylated with endoH as described previously (Frandsen *et al.*, 2016; Simmons *et al.*, 2017; Tandrup *et al.*, 2020). The protein sample was pre-incubated with Cu^{2+} acetate in equimolar amounts for 1 h at 4°C prior to setup. Crystals of *Ls*AA9_A(f) were grown *via* sitting-drop vapour diffusion. Crystallization and optimization of the crystals has been described previously (Frandsen *et al.*, 2016). The two crystals used for determining 12 of the structures presented here were grown with a reservoir consisting of 3.3 *M* NaCl and 0.1 *M* citric acid at pH 3.5. Drop and reservoir volumes were 0.5 and 100 µl, respectively, with a drop composition of 0.3 µl protein (19 mg ml^{-1} in 20 m*M* sodium acetate pH 5.5), 0.1 µl reservoir and 0.1 µl milli-Q water. Crystals appeared within 2 d. Prior to harvesting, the crystals were moved to a drop of 3.0 *M* NaCl and 0.1 *M* citric acid at pH 5.5 for 10 min to ensure an ordered active site (Frandsen *et al.*, 2017). Subsequent soaking with oligosaccharide ligand was done for one of the crystals by moving it to a drop containing 3.0 *M* NaCl, 0.1 *M* citric acid pH 5.5, as well as 1.0 *M* of Cell$_4$ for 10 min. Crystals were flash frozen in liquid nitrogen without any added cryoprotectant.

The *Ls*AA9_A(f) crystal used for ascorbic acid soak was grown in a VDX plate (Hampton Research) by hanging-drop vapour diffusion. The crystal was grown in a 2 µl drop of 1.5 µl 3.5 *M* NaCl, 0.1 *M* citric acid pH 4.0 and 0.5 µl enzyme (23 mg ml^{-1} in 20 m*M* Na acetate pH 5.5), with a reservoir of 1 ml. After growing a crystal of approximately 200 µm in each dimension, it was transferred to a drop consisting of 3.5 *M* NaCl, 0.1 *M* citric acid pH 5.5, 0.01 *M* ascorbic acid pH 5.5 for 20 min before flash freezing.

For room-temperature data, an *Ls*AA9_A(f) crystal was grown using 15 µl 20.8 mg ml^{-1} enzyme (Cu-loaded using Cu acetate in equimolar amounts) in 5 µl 3.0 *M* NaCl, 0.1 *M* citric acid pH 3.5 in a VDX plate (Hampton Research). The crystal grew to approximately 200 µm in each dimension within a few weeks and was transferred to a solution of 3.0 *M* NaCl, 0.1 *M* citric acid pH 5.5 for 10 min before being mounted on a cryo-loop (MiTeGen). A MicroRT capillary (MiTeGen) was prepared to contain 20 µl of 3.0 *M* NaCl, 0.1 *M* citric acid pH 5.5. The cryo-loop-mounted crystal was inserted into the MicroRT capillary to prevent the crystal from drying during data collection.

A room-temperature data set was collected at the BioMAX beamline of the MAX IV Laboratory from a crystal grown in 0.1 µl 3.0 *M* NaCl, 0.1 *M* citric acid pH 3.5 and 0.3 µl 19 mg ml^{-1} *Ls*AA9_A(f), also Cu-loaded. The crystal was equilibrated for pH, as above. The crystal was mounted in a 1.0 mm diameter glass capillary (WJM glass), plugged with 3.0 *M* NaCl, 0.1 *M* citric acid pH 5.5 in both ends and sealed with beeswax.

*Ls*AA9_A(*Ec*) was produced in *E. coli* using the LyGo platform with the pLyGo-*Ec*-6 expression vector (Hernández-Rollán *et al.*, 2021). The sample was purified using Q-Sepharose anion-exchange chromatography with a column equilibrated with 25 m*M* Bis-Tris pH 5.87. The sample was eluted using the same buffer over a 0–500 m*M* NaCl gradient. The protein, in 25 m*M* Bis-Tris pH 5.87 and 175 m*M* NaCl, was

initially screened for crystallization conditions at a concentration of 1.83 mg ml^{-1} in 0.3 µl drops (3:1 and 1:1 protein-to-reservoir ratio) with the commercially available Index (Hampton Research), PACT (Qiagen) and JCSG+ (Molecular Dimensions) crystallization screens. At least 30 min before crystallization setup, equimolar quantities of acetate were added to the enzyme sample. Crystals were formed at room temperature in the A2 conditions of the Index screen [0.1 *M* sodium acetate trihydrate pH 4.5, 2.0 *M* (NH$_4$)$_2$SO$_4$], which was further optimized to 0.1 *M* sodium acetate pH 4.5 and 1.8 *M* (NH$_4$)$_2$SO$_4$. Crystals grown under this condition were flash frozen without added cryoprotectant.

An initial oligosaccharide-binding structure of *Ls*AA9_A(*Ec*)-Cell$_3$ was obtained from a crystal soaked for 30 min in a 3 µl drop suspended over a reservoir with 100 µl 2 *M* (NH$_4$)$_2$SO$_4$ and 0.1 *M* sodium acetate in a VDX plate. The drop consisted of 16% glycerol, 0.3 *M* Cell$_3$ and *Ls*AA9_A(*Ec*) protein stock to facilitate a final concentration of 0.3 mg ml^{-1}. The soaked crystals were mounted in fibre loops and flash frozen.

Crystals of *Ls*AA9_A(*Ec*) soaked in cellotetraose (Cell$_4$) were grown by the batch crystallization method in 1.5 ml microfuge tubes (Fisher Scientific) using a 1.8 mg ml^{-1} protein concentration. The crystallization condition was 2.3 *M* (NH$_4$)$_2$SO$_4$, 0.1 *M* sodium acetate pH 4.2. A 200 µl batch was set up at 4°C with the protein and the crystallization condition in a 1:3 ratio. The crystals appeared within 4 d. For soaking, 0.5 µl of the crystal slurry was added to a drop containing 0.05 *M* Cell$_4$ in the crystallization condition with 18% glycerol and incubated from 5 to 30 min. The crystals were then flash frozen in liquid nitrogen.

The crystals of *Ls*AA9_A(*Ec*) used for photoreduction were grown in microbatch crystallization plates. Crystals not soaked in substrate were grown in 4 µl drops composed of 3 µl 2.0 *M* (NH$_4$)$_2$SO$_4$, 0.1 *M* sodium acetate pH 4.5 and 1 µl *Ls*AA9_A(*Ec*) (1.8 mg ml^{-1} in 25 m*M* Bis-Tris pH 5.8 175 m*M* NaCl). Crystals soaked in Cell$_3$ were grown in 3 µl drops composed of 2 µl 2.0 *M* (NH$_4$)$_2$SO$_4$, 0.1 *M* sodium acetate pH 4.5 and 1 µl *Ls*AA9_A(*Ec*) (1.8 mg ml^{-1} in 25 m*M* Bis-Tris pH 5.8, 175 m*M* NaCl). The drops were covered in a layer of paraffin and silicon oils in a paraffin–silicon ratio of 3:2. The drops were set up at 4°C and crystals appeared within 4 d. Crystals used in a soaking experiment were moved into a drop containing 0.5 *M* Cell$_3$, 2.0 *M* (NH$_4$)$_2$SO$_4$ and 0.1 *M* sodium acetate pH 4.5. Prior to flash freezing in liquid nitrogen, the crystals were cryoprotected in 20%(*w*/*v*) glycerol, 2.0 *M* (NH$_4$)$_2$SO$_4$, 0.1 *M* sodium acetate pH 4.5.

*Ta*AA9_A was produced as described in Harris *et al.* (2010) and purified using Q-Sepharose anion-exchange chromatography with a column equilibrated with 20 m*M* Tris pH 6.0. *Ta*AA9_A was eluted in the same buffer over a 0.79–2.5 m*M* NaCl gradient. The sample was deglycosylated in 20 m*M* MES pH 6.0, 125 m*M* NaCl by incubation with ~0.05 units per mg *Ta*AA9_A of endoH (Roche Diagnostics, 11643053001), and then buffer exchanged to 20 m*M* Na acetate pH 5.5. Prior to crystallization the sample was incubated for 1 h with equimolar amounts of Cu acetate. Crystals of *Ta*AA9_A were grown in 0.4 µl drops composed of 0.3 µl *Ta*AA9_A

Table 1
The final data sets derived from data collected at increasing photon flux on LsAA9_A(f) crystals.

The 7.88×10^3 Gy data set consists of the first 45° of the collection at 10^{10} photons/s. The 5.99×10^4 Gy data set consists of the last 45° of the collection at 10^{10} photons/s. The 1.39×10^5 Gy data set consists of the first 45° of the 10^{11} photons/s collection. The 3.60×10^5 Gy data sets consists of images in the range 100–180° of the 10^{11} photons/s collection. The 1.45×10^6 Gy data sets consists of the first 45° of the 10^{12} photons/s collection. Finally, the 6.65×10^6 Gy data set is from the last 45° of the 10^{12} photons/s collection.

Photon flux	10^{10} photons/s		10^{11} photons/s		10^{12} photons/s	
Data range used (°)	0–45	315–360	0–45	100–180	0–45	315–360
X-ray dose (Gy)	7.88×10^3	5.99×10^4	1.39×10^5	3.60×10^5	1.45×10^6	6.65×10^6

(15.9 mg ml^{-1} in 20 mM sodium acetate pH 5.5) and 0.1 µl 0.02 M MgCl$_2$, 0.1 M HEPES pH 7.5, 22%(w/v) polyacrylic acid 5100 sodium salt.

2.2. Single-crystal X-ray data collection, structure determination and refinement

Data for the initial structure determination of LsAA9_A(Ec) were collected at 100 K at the BioMAX beamline at MAX IV (Lund, Sweden) (Ursby $et\ al.$, 2020). The images were collected for 360° with an oscillation of 0.1° and a 100 ms exposure time for each image using a wavelength of 1.1 Å. The BioMAX beamline was also used to collect 360° data with an oscillation of 0.1° and an 11 ms exposure time for each image for LsAA9_A(Ec)-Cell$_4$ crystals. The autoprocessed (autoPROC pipeline) reflection file was used for structure determination. The highest resolution cut-off of diffraction data was generally chosen based on a CC$_{1/2}$ in the outer shell of above 50%.

For LsAA9_A(f), a data set was collected at room temperature using an in-house diffractometer at the Oak Ridge National Laboratory. The set-up consisted of a Rigaku HighFlux HomeLab instrument with a MicroMax-007 HF X-ray generator and an EIGER R 4M detector. Data were collected for 98° with 0.25° oscillation and a 10 s exposure per image. The data were processed using $CrysAlis\ PRO$ (Rigaku) and scaled using $AIMLESS/POINTLESS$ (Evans & Murshudov, 2013; Evans, 2006). Room-temperature data were also collected for LsAA9_A(f) at the BioMAX beamline of the MAX IV synchrotron. The glass capillary mounted sample was illuminated with X-rays for 360° with an oscillation of 0.1° and an exposure per frame of 0.01 s. The data were processed using $XDS/XSCALE$.

Data for the photoreduction study were collected at the P11 beamline of PETRA-III at DESY, Hamburg (Burkhardt $et\ al.$, 2016). For each of the data sets, images were collected for 360° with an oscillation of 0.1° and a 100 ms exposure time for each image. Three data sets were collected on LsAA9_A(f) and LsAA9_A(f)-Cell$_4$ with the beam transmission set to 1, 10 and 100%. This corresponded to estimated photon fluxes of 10^{10}, 10^{11} and 10^{12} photons/s, respectively. Each data collection was performed without changing the crystal orientation between collections. Subsets of the three data sets (two for each) were processed with the fewest number of images possible for a completeness of ~90%. The number of images for each data set was limited in an effort to trap the structures with a specific oxidation state of the Cu, thus being the basis for six structures

per crystal, each at a different dose. The structures corresponding to the LsAA9_A(f) data sets were solved according to Table 1. The collection strategy was identical between the data sets collected from substrate-free crystals, and crystals soaked in Cell$_4$. For both the LsAA9_A(f) structures with and without substrate, anomalous signal could be used to determine the absence/presence of Cl$^-$ at the active site.

Data-collection parameters for the photoreduction of crystals of LsAA9_A(Ec) and TaAA9_A were chosen to approximately match the relative doses received by the LsAA9_A(f) crystals described above. Using $RADDOSE3D$ (Zeldin $et\ al.$, 2013), the average diffraction weighted dose was calculated prior to X-ray exposure to find the optimal flux required to achieve similarly reduced active-site Cu in the resulting structures and calculated again after the experiment for a final dose.

Data for the photoreduction study were also processed and scaled using $XDS/XSCALE$ (Kabsch, 2010). The lowest dose data sets were used as references during the processing of higher dose data sets to ensure consistent indexing. The highest resolution cut-off was generally chosen based on a CC$_{1/2}$ in the outer shell of above 40%. The consequence of following the set scheme in Table 1 was that in some cases a completeness of less than 100% and a data redundancy <2 were obtained, but this was considered a reasonable trade-off for consistency. Phases for LsAA9_A(f) were obtained from the previously published high-resolution LsAA9_A(f) structure (PDB entry 5ach) (Frandsen $et\ al.$, 2016). For LsAA9_A(Ec), the space group was different than for LsAA9_A(f), and the phases were obtained using $MOLREP$ (Vagin & Teplyakov, 1997) and PDB entry 5ach as the search model. Phases for LsAA9_A(Ec)-Cell$_4$ and Cell$_3$ were obtained from the isomorphous oligosaccharide-free structures. For TaAA9_A, the phases were obtained from the previously published high-resolution TaAA9_A structure with a single molecule in the asymmetric unit (PDB entry 3zud) (Quinlan $et\ al.$, 2011).

For all structures, rigid-body and restrained refinement were performed in $REFMAC5$ (Murshudov $et\ al.$, 1997) of the CCP4 suite (Winn $et\ al.$, 2011), alternated with manual rebuilding and validation performed in $Coot$ (Emsley & Cowtan, 2004). Further validation was performed using $BAVERAGE$ and $PROCHECK$ (Vaguine $et\ al.$, 1999) of the CCP4 suite (Winn $et\ al.$, 2011). For data collection and refinement statistics, see Tables S1–S6 in the supporting information. Figures of the resulting models were prepared in

PyMOL (*The PyMOL Molecular Graphics System*; Version 2.0.4; Schrödinger, LLC). The active-site distances and angles of the final models were measured in *Coot* and using the Python library Biopython (Cock *et al.*, 2009). Animations of active-site changes during photoreduction (see Movies S1–S5 in the supporting information) were made in *PyMOL* using the *morph* feature with no trajectory refinement.

2.3. Serial synchrotron crystallography

The *Ls*AA9_A(f)-SSX data set was collected at the ID29 beamline (de Sanctis *et al.*, 2012) of the European Synchrotron Radiation Facility (ESRF). The data were collected using the *Mesh & Collect* routine (Zander *et al.*, 2015), in a similar manner to that described recently for *Ao*AA13 (Muderspach *et al.*, 2019). For each crystal identified by the routine, data were collected over a total rotation of 10°, though only 2.5° were used for processing, with an oscillation of 0.1° per image at a wavelength of 0.98 Å. 13 data sets were processed individually with identical parameters using *XDS* (Kabsch, 2010). The hierarchical cluster analysis software *ccCluster* (Santoni *et al.*, 2017) was used to determine which data sets could be merged and scaled based on their correlation coefficient distances. The resulting data set from this merge was used to solve the *Ls*AA9_A(f)-SSX structure. Phasing and refinement were performed as described above.

3. Results and discussion

3.1. Overall structure overview for this study

This study includes five LPMO and substrate combinations with similar photoreduction protocols at cryogenic temperatures: *Ls*AA9_A produced in two recombinant systems giving different post-translational modifications and crystallized under different conditions in different space groups, in the presence/absence of oligosaccharide ligands, and *Ta*AA9_A (without the oligosaccharide ligand). Table 2 summarizes the post-translational modifications, crystallization solution compositions, crystal form characteristics and exogenous ligands for the five combinations investigated. *Ls*AA9_A and *Ta*AA9_A display the immunoglobin G-like β-sandwich fold observed for all LPMOs structurally characterized so far [see Figs. 1(*b*) and 1(*c*)]. The catalytic Cu ion is coordinated by the His-brace, fitting an elongated octahedral geometry, and lies in the middle of a relatively flat surface (Frandsen & Lo Leggio, 2016; Vu & Ngo, 2018; Tandrup *et al.*, 2018), where the polysaccharide substrate has been demonstrated experimentally to bind in several AA9 LPMOs (Frandsen *et al.*, 2016; Tandrup *et al.*, 2020; Courtade *et al.*, 2016). In both proteins, a tyrosine –OH group functions as one of the axial ligands to the Cu. In oligosaccharide-free *Ls*AA9_A(f), the copper coordination sphere includes two water ligands in equatorial (eq) and axial (ax) positions (see Fig. 1). The chemical nature of the exogeneous equatorial and axial ligands changes depending on the crystallization conditions and the exogenous axial ligand is displaced upon oligosaccharide binding.

The bacterially expressed *Ls*AA9_A(*Ec*) has recently been shown to be fully active (Brander, Tokin *et al.*, 2021) and was also used in a high-resolution study to determine the protonation stages in the second coordination sphere of Cu (Banerjee *et al.*, 2022). The structure of *Ls*AA9_A(*Ec*) is very similar to the previously published fungally expressed *Ls*AA9_A(f) structures (all-atom r.m.s. deviation for resting-state substrate-free structures: overall = 0.56 Å and His-brace = 0.10 Å), except for post-translational modifications and differences in the exogenous ligands to the Cu due to different crystallization conditions (Table 2 and Fig. S1).

The crystal packing around the substrate-binding site differs between the *Ls*AA9_A(*Ec*) and *Ls*AA9_A(f) crystal forms. *Ls*AA9_A(f) has an unrestricted binding site, so that *Ls*AA9_A(f) crystals soaked in Cell$_4$ in this study bind from subsite −2 to +2, as reported previously (Tandrup *et al.*, 2020). In contrast, the −2 binding subsite of *Ls*AA9_A(*Ec*) is blocked by crystal contacts. This prevents binding in the same mode observed previously for *Ls*AA9_A(f) for both Cell$_3$ and Cell$_4$ (Frandsen *et al.*, 2016; Tandrup *et al.*, 2020). In the structure of *Ls*AA9_A(*Ec*)-Cell$_4$, the substrate is modelled from subsite −1 to +3, with the glucose monomer in the +3 subsite being partially disordered (see Figs. S2 and S3). Thus, we have chosen *Ls*AA9_A(*Ec*)-Cell$_3$ as a model for the photoreduction study. In this structure, Cell$_3$ is bound at subsites −1 to +2. In line with previous structural studies (Frandsen *et al.*, 2016), the binding of oligosaccharides expels the axial water molecule, thus only the equatorial exogenous ligand remains. A Cl$^-$ ion occupies this position where O$_2$ or H$_2$O$_2$ are expected to bind during the reaction. For *Ls*AA9_A(f), this is likely due to the high NaCl concentration in the crystallization conditions (upwards of 3.0 *M*), while for *Ls*AA9_A(*Ec*), the NaCl concentration is much lower. Anomalous signal, routinely used to detect heavy atoms in crystals, could only determine the presence of Cl$^-$ unambiguously in *Ls*AA9_A(f)-Cell$_4$ structures (not shown), but Cl$^-$ still fits the observed electron density more accurately for *Ls*AA9_A(*Ec*)-Cell$_3$, compared to water and SO$_4^{2-}$.

The structure of *Ta*AA9_A presented here is similar to those reported previously (PDB entries 3zud and 2yet) (Quinlan *et al.*, 2011), except that the active-site copper is well defined and free of the disorder observed previously. *Ta*AA9_A has been used previously in describing the LPMO active site in theoretical studies (Hedegård & Ryde, 2018; Kjaergaard *et al.*, 2014; Kim *et al.*, 2014) and the structures here could therefore present an improvement for further calculations. Crystal contacts most likely prevent binding at negative subsites, assuming the oligosaccharide binds in a similar manner to previous oligosaccharide-binding structures with *Ls*AA9_A and an AA9 from *Collariella virescens* (*Cv*AA9_A) (Frandsen *et al.*, 2016; Simmons *et al.*, 2017; Tandrup *et al.*, 2020), and it has not been possible so far to obtain an oligosaccharide bound in the structure of this protein, which also has no reported activity on oligosaccharides.

Crystals of fungal and bacterially expressed *Ls*AA9_A (unsoaked and soaked in Cell$_4$ and Cell$_3$ oligosaccharide,

Table 2
A brief overview of the proteins and crystals used in this study.

Protein	PDB entry	Post-translational modification	Oligo-saccharide ligand	Occupied binding subsites	Mother liquor composition	Protein buffer	Space group	No. of molecules in asymmetric unit	Maximum resolution in this study (Å)	Non-H_2O exogenous ligands
LsAA9_A LsAA9_A(f)	7pxi 7pxj 7pxk 7pxl 7pxm 7pxn	His1 $N^{\varepsilon 2}$ methylation; N-glycosylation on Asn33			3.3 M NaCl, 0.1 M citric acid pH 3.5	50 mM sodium acetate pH 5.5	$P4_132$	1	1.30	
LsAA9_A LsAA9_A(f)	7pyd 7pye 7pyf 7pyg 7pyh 7pyi	His1 $N^{\varepsilon 2}$ methylation; N-glycosylation on Asn33	1.0 M cellotetraose	$-2 - 1 +$ $1 + 2$	3.3 M NaCl, 0.1 M citric acid pH 3.5	50 mM sodium acetate pH 5.5	$P4_132$	1	1.90	Cl^-†
LsAA9_A LsAA9_A(Ec)	7pyl 7pym 7pyn 7pyo 7pyp 7pyq	‡			2.3 M $(NH_4)_2SO_4$, 0.1 M sodium acetate pH 4.5	25 mM Bis-Tris pH 5.8, 175 mM NaCl	$P4_1$	1	1.30	SO_4§
LsAA9_A LsAA9_A(Ec)	7pyu 7pyw 7pyx 7pyy 7pyz 7pz0	‡	0.5 M cellotriose	$-1 + 1$ $+ 2$¶	2.3 M $(NH_4)_2SO_4$, 0.1 M sodium acetate pH 4.5	25 mM Bis-Tris pH 5.8, 175 mM NaCl	$P4_1$	1	1.20	Cl^-†
TaAA9_A	7pz3 7pz4 7pz5 7pz6 7pz7 7pz8	His1 $N^{\varepsilon 2}$ methylation; N-glycosylation on Asn138			20 mM $MgCl_2$, 0.1 M HEPES pH 7.5, 22%(w/v) polyacrylic acid 5100 sodium salt	50 mM sodium acetate pH 5.5	$P2_1$	1	1.40	Acrylic acid§

† Cl present from crystallization conditions is often found in substrate-bound structures and is expected to inhibit the position binding either O_2 or H_2O_2 (Frandsen *et al.*, 2016). ‡ LsAA9_A(Ec) is lacking the N-terminal His methylation, as expected from the bacterial expression (Fig. S1) § Not coordinating directly to Cu. Present from crystallization conditions. ¶ Cellotriose is also bound in a pocket at β-sheet 4 (Fig. S2). Binding in this pocket is not believed to have any biological relevance.

respectively) and crystals of TaAA9_A were exposed to X-rays for three consecutive data collections, with an increasing flux of photons, and from these, images were selected to form data sets for structure determination at individual X-ray doses. The images in each data set were limited to the minimal amount necessary to solve the structures while still obtaining a complete and statistically reasonable data set (see *Methods* section for details of the data reduction and Tables S1–S6 for statistics). We solved two structures from each of the three collections for all the crystals, giving snapshots at six X-ray doses for each. Two additional low-dose structures for the study come from the data for LsAA9_A(f) at room temperature (RT) from an in-house diffractometer and synchrotron to resolution limits of 1.8 and 1.9 Å, respectively (see Fig. S4). As a reference for the Cu$^+$ state, we used a chemically reduced structure obtained from LsAA9_A(f) crystals soaked in 10 mM ascorbic acid.

These reference structures were used to establish which parameters should be monitored to follow the transition from Cu^{2+} to Cu$^+$. Previously, a tendency towards a slight increase in the Cu—His1-N distances and slight decreases in the Cu—

His1 $N^{\delta 1}$ and Cu—His $N^{\varepsilon 2}$ distances have been reported on photoreduction (Gudmundsson *et al.*, 2014). However, as can be seen in Table 3, the differences are very small between our Cu^{2+} and Cu$^+$ reference structures. The transition from Cu^{2+} to Cu$^+$ can instead be followed more clearly by measuring the interatomic distances between Cu and its ligands (see Table 3), including the equatorial and axial water molecules (see Fig. 1). In terms of distances, we here define the Cu state based on distances <2.2, 2.2–2.9 and >2.9 Å between Cu and the equatorial ligand as Cu^{2+}, a mix and Cu$^+$, respectively. For the axial Cu ligand, the distances are defined here as <2.7, 2.7–3.2 and >3.2 Å, respectively. While due to Jahn–Teller distortion (Jahn & Teller, 1937) even longer distances have been observed, at distances longer than these we can probably be confident that there is no longer a coordination bond. Compared to earlier studies on LPMOs, the lowest-dose Cu–water ligand distances found here are slightly longer than for other type II Cu sites investigated using X-ray doses in a similar range (Frankaer *et al.*, 2014). For reference, in aqueous six-coordinated complexes of Cu^{2+}, equatorial water molecules are at a distance of around 2.0 Å from the ion and axial water molecules are up to

Table 3
Structural parameters within the LPMO Cu site.

The lowest and highest X-ray dose structures are listed, together with additional reference structures. Distances (between the indicated atom and Cu) and angles were measured in *Coot* (Emsley & Cowtan, 2004) and using the *Biopython* module (Cock *et al.*, 2009). In cases where a ligand atom is modelled in a double conformation, the distance is an average weighted by the occupancy of the atom. Further structural parameters for all structures are presented in Tables S7 and S8. Res = high-resolution limit. Distances are measured from Cu to the indicated atom. $\theta_1, \theta_2, \theta_3$ and θ_T (°) are defined in Vu & Ngo (2018). The lowest/highest/average distance and $\theta_1, \theta_2, \theta_3$ and θ_T (°) for Cu^{2+}/Cu^+ structures are from Vu & Ngo (2018). ECR = estimated coordinate error based on the R value; value extracted from the *REFMAC5* output PDB file.

	PDB entry	Dose (Gy)	Res. (Å)	R_{work}/R_{free} (%)	$N^{\delta1}$ (Å)	N_{Am} (Å)	$N^{\varepsilon2}$ (Å)	O_{Tyr} (Å)	Eq (Å)	Ax (Å)	$\theta_1, \theta_2, \theta_3$ (°)	θ_T (°)	ECR (Å)
LsAA9_A(f) (RT)	7pxr		1.80	14.67/16.62	1.9	2.2	2.0	2.8	2.2	2.8	88.6, 92.9, 176.6	3.3	0.081
LsAA9_A(f) (RT-sync)	7pxs	1.91×10^3	1.90	16.94/19.56	1.9	2.2	2.0	2.8	2.2	2.6	92.7, 94.7, 170.5	5.9	0.106
LsAA9_A(f) (Ascorbic acid)	7pxu	2.08×10^3	1.80	19.52/22.65	1.9	2.3	2.0	2.9	4.0	3.7	94.8, 96.3, 168.4	3.4	0.119
	7pxv	1.70×10^7	1.50	18.74/20.70	1.8	2.3	2.0	2.8	4.0	3.5	93.2, 97.4, 168.6	4.4	0.063
LsAA9_A(f)	7pxi	7.88×10^3	1.57	18.30/20.99	1.9	2.2	2.0	2.7	2.2	2.7	92.9, 89.6, 177.1	1.5	0.080
	7pxn	6.65×10^6	1.65	20.35/22.18	1.9	2.3	2.0	2.7	3.3	3.3	91.7, 99.7, 167.5	5.1	0.057
LsAA9_A(Ec)	7pyl	1.49×10^4	1.70	14.83/18.83	2.0	2.1	2.0	2.7	1.9	2.6	91.8, 94.9, 172.6	3.3	0.094
	7pyq	6.35×10^6	1.60	14.42/16.78	2.0	2.2	2.0	2.8		3.8	93.3, 102.9, 162.0	7.8	0.069
LsAA9_A(f) (SSX)	7pxt	7.02×10^4	2.40	18.67/24.76	1.9	2.3	1.9	2.7	3.9	2.9	84.9, 99.6, 171.5	7.1	0.319
TaAA9_A	7pz3	5.37×10^3	1.90	20.81/25.63	1.9	2.2	2.1	3.0	2.2	2.0	94.0, 91.4, 174.6	−1	0.207
	7pz8	3.12×10^6	1.40	15.12/16.89	1.9	2.2	2.0	2.9	2.5	3.0	94.6, 96.1, 169.3	1	0.055
LsAA9_A(f)-Cell$_4$	7pyd	7.88×10^3	2.21	22.47/28.71	2.0	2.3	2.0	2.5	2.3		96.4, 94.1, 161.1	15.6	0.246
	7pyi	6.65×10^6	2.05	21.80/26.00	1.9	2.5	2.0	2.7	3.8		98.1, 110.1, 147.9	14.5	0.184
LsAA9_A (Ec)-Cell$_3$	7pyu	1.49×10^4	1.40	14.19/16.22	2.0	2.1	2.0	2.6	2.3		91.3, 91.7, 169.2	10.4	0.052
	7pz0	9.81×10^6	1.20	13.40/14.75	1.9	2.3	1.9	2.7	3.8		93.0, 98.8, 165.7	8.2	0.030
LsAA9_A(Ec)-Cell$_4$	7pxw	2.14×10^6	1.40	11.71/15.98	2.0	2.3	2.0	2.7	3.9		92.4, 99.5, 165.3	8.5	0.047
Cu^{2+}													
Lowest					2.1	1.9	1.9				88, 85, 168	−2.4	
Highest					2.4	2.3	2.4				103, 96, 178	4.2	
Average					2.2	2.0	2.1				93, 92, 174	0.75	
Cu^+													
Lowest					2.0	1.9	1.9				93, 93, 155	−14	
Highest					2.3	2.1	2.3				99, 103, 169	16	
Average					2.2	2.0	2.0				96, 99, 163	3.9	

0.3 Å longer (de Almeida *et al.*, 2009). These distances have been used previously to examine the active-site geometry of LPMOs (Vu & Ngo, 2018), and the definitions of distance magnitudes are based on previous LPMO studies and small-molecule Cu complexes (Gudmundsson *et al.*, 2014; Vu & Ngo, 2018; Persson, 2010). Based on these cut-offs, our reference low-dose LsAA9_A(f) structure is very close to a full Cu^{2+} state. For the chemically reduced crystals, structures at two X-ray doses were obtained (a low dose of 2.08×10^3 Gy and a high dose of 1.70×10^7 Gy) (see Fig. S5). Consistent with a fully Cu^+ state, the distances to the equatorial and axial water molecules are large even at low dose (4.0 and 3.7 Å) and do not increase with dose (4.0 and 3.5 Å, respectively) (see Table 3 for all measured active-site distances).

Upon reduction of the metal from Cu^{2+} to Cu^+, the geometry is expected to change from a trigonal bipyramid, distorted square pyramid, seesaw or elongated octahedral geometry (the latter applicable to the AA9 LPMOs studied here) towards a T-shaped geometry, with increased deviations from 90° in the defined angles θ_1 and θ_2, a decrease in θ_3 and an increase in θ_T [see Fig. 1(d)] (Vu & Ngo, 2018). The $\theta_1, \theta_2, \theta_3$ and θ_T values in the chosen reference structures are consistent with the previous findings for the geometrical differences between Cu^{2+} and Cu^+ geometries, and a steady increase in θ_2 and a decrease in θ_3 are the clearest trends which are common to the three types of crystals investigated. We have further

observed a decrease in θ_{H-H} and θ_{H1}, with an increase in θ_{HN} in the fully chemically reduced structures compared to the reference Cu^{2+} structure (see Fig. S6). Most angles do not change upon continued exposure of the chemically reduced LsAA9_A(f), except θ_{H1} and θ_{H-H}, which decrease further (see Table S7). Thus, all these angles have also been monitored through the photoreduction studies as useful indicators of the Cu ion state (Tables S7 and S8).

3.2. Photoreduction of substrate-free AA9s

The lowest dose LsAA9_A(f) cryotemperature structure was solved from a data set totaling a dose of 7.88×10^3 Gy [Figs. 1 and 2(a)]. Detailed transitions (all X-ray doses) can be seen in Figs. S7 and S8, and Movies S1 and S2, while different geometrical parameters under photoreduction are monitored in Figs. S6 and S9. Efforts were made to expose other crystals to comparable doses. For LsAA9_A(Ec), the lowest dose was 1.49×10^4 Gy [Fig. 2(c)]. In both cases, the active-site distances and angles agree well with a Cu^{2+} oxidation state of type II Cu (Vu & Ngo, 2018; Solomon *et al.*, 2014; Frandsen *et al.*, 2016) [see Figs. 2(a) and 2(c)], although θ_3 and θ_T may indicate that photoreduction has started for LsAA9_A(Ec), which is collected at a slightly higher dose. In all the low-dose structures, Cu has been modelled in full occupancy. The distance between Cu and the equatorial water is 0.2 Å shorter

in *Ls*AA9_A(*Ec*) and is probably affected by a nearby sulfate ion at a hydrogen-bond distance of 2.5 Å. The key measured geometrical parameters are presented in Table 3, with an additional analysis in Tables S7 and S8. In the lowest-dose substrate-free structures of fungal/bacterial *Ls*AA9_A, the distance to the equatorial water ligand is in the range 2.2–2.3 Å, while that to the axial ligand is in the range 2.6–2.7 Å. For comparison, QM/MM models have shown distances of 2.16/2.25, 2.08/2.53 and 2.21/2.34 Å for the equatorial/axial water molecule, depending on the parameters of the calculation (Theibich *et al.*, 2021), which could indicate that even at the lowest X-ray dose possible, a small amount of photoreduction has occurred.
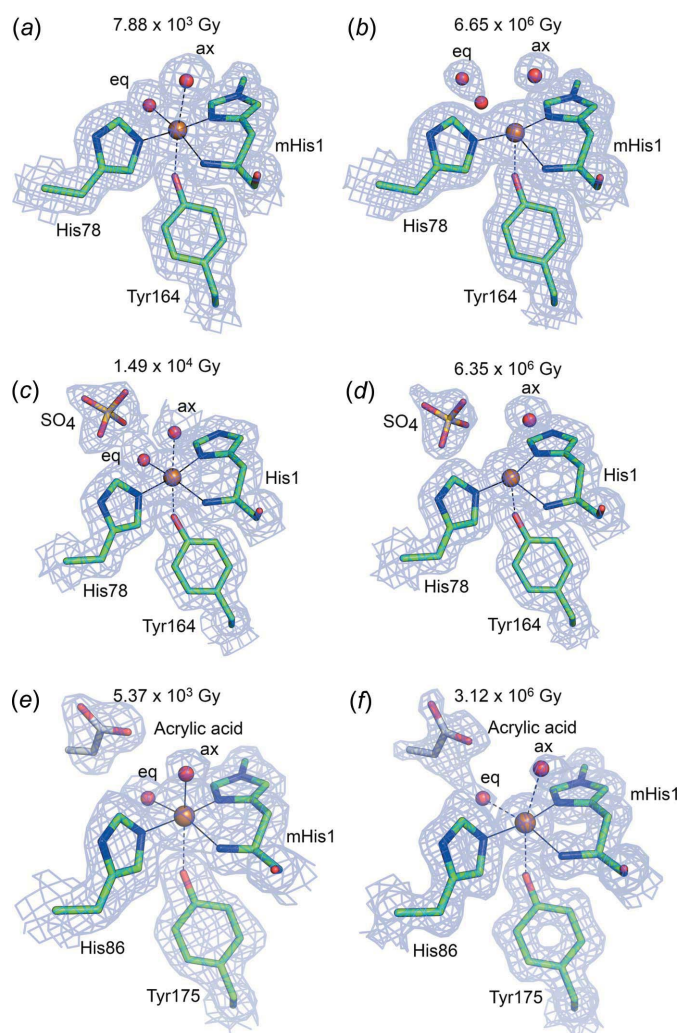
Figure 2
LPMO Cu sites in *Ls*AA9_A(f), *Ls*AA9_A(*Ec*) and *Ta*AA9_A at the lowest and highest X-ray doses. *Ls*AA9_A(f) at (*a*) low and (*b*) high dose. *Ls*AA9_A (*Ec*) at (*c*) low and (*d*) high dose. *Ta*AA9_A at (*e*) low and (*f*) high dose. The distances between Cu (orange spheres) and the equatorial/axial water molecules (red spheres) increase with increasing X-ray dose in the transition from Cu^{2+} to Cu^+. In some cases, the water molecules have been modelled in a double conformation (*b*) or left unmodelled due to a lack of electron density (*d*). Distances below 2.2/2.7 Å are shown as full lines (coordination distance), below 2.9/3.2 Å as dashed lines (close to coordination distance) and above 2.9/3.2 Å with no line (not coordinating) for the equatorial/axial ligands, respectively. $2F_o–F_c$ electron density is shown at a 1.0 contour level as blue mesh.

As the X-ray dose increases, so do the distances to the exogenous water ligands, which gradually become disordered and/or disappear, as expected (see Fig. 3). For all intermediate doses of *Ls*AA9_A(f), the equatorial water molecule has been modelled in a double conformation, each with 50% occupancy. For *Ls*AA9_A(*Ec*), the equatorial water molecule becomes disordered at an X-ray dose above 3.33×10^5 Gy, where the molecule can no longer be modelled confidently. At intermediate doses of *Ls*AA9_A(*Ec*), the axial water is modelled in a double conformation, each with 50% occupancy, or in an alternative conformation with sulfate (see Fig. S8), likely hindering the migration of the water.

Both *Ls*AA9_A(f) and *Ls*AA9_A(*Ec*) structures with the highest X-ray doses (6.65×10^6 and 6.35×10^6 Gy, respectively) exhibit exogenous ligand distances and other parameters agreeing with a predominant Cu^+ state, as reported previously (Vu & Ngo, 2018; Gudmundsson *et al.*, 2014; Frandsen *et al.*, 2016) and in agreement with our chemically reduced *Ls*AA9_A(f) structures. In *Ls*AA9_A(f), both the axial and the equatorial water molecules have increased distances from Cu compared to the lowest dose (0.6 Å more for the axial and 1.2 Å more for the equatorial) and >3.3 Å from Cu. Thus, the Cu atom has effectively lost its two ligands when reduced from Cu^{2+} to Cu^+ [see Table 3 and Figs. 2(*b*) and S7]. In the higher-dose structures, the equatorial water molecule has migrated away from the Cu ion and is coordinated by Gln162 and/or His147 of the secondary coordination sphere instead (Fig. S10). In *Ls*AA9_A(*Ec*), there is no residual density for the equatorial water at the highest dose, while the axial water is 0.5 Å further away than in the lowest dose. Compared to the chemically reduced crystals, the measured Cu-site distances are shorter even in the highest dose *Ls*AA9_A(f) structure. This might imply that the *Ls*AA9_A(f) structure is not fully reduced and that it may indeed be difficult to fully photoreduce an LPMO. Alternatively, photoreduction at 100 K may impede full migration of bound water.

Looking at the θ angles in the two substrate-free *Ls*AA9_A variants (Figs. 4 and S6), Cu reduction is associated with an increase in θ_2, θ_T and θ_{HN} (>8, >3 and >3°, respectively). Additionally, a decrease in θ_3, $\theta_{H–H}$ and θ_{H1} (>9, >3 and >9°, respectively) can be observed over the transition, although the absolute values between the two enzymes differ somewhat.

In a previous EXAFS study, it was indicated that the Cu^{2+} structure of *Ta*AA9_A could be well represented by four N/O ligands at an average distance from Cu of 1.98 Å (Kjaergaard *et al.*, 2014), whereby one of the close ligands was lost on photoreduction, leaving the Cu atom in a T-shaped coordination. The equatorial ligand distances in the lowest-dose *Ta*AA9_A structure presented have an average of 2.1 Å, which is within the agreement level that can be expected given an estimated coordinate error of 0.207 Å for this structure (see Table 3); however, in the crystal structure, an axial water is additionally very close at a distance from Cu of 2.0 Å and is significantly closer than in the *Ls*AA9_A substrate-free structures above. The distance increases steadily with dose to 3.0 Å [see Figs. 2(*e*) and 2(*f*), with a more detailed transition in
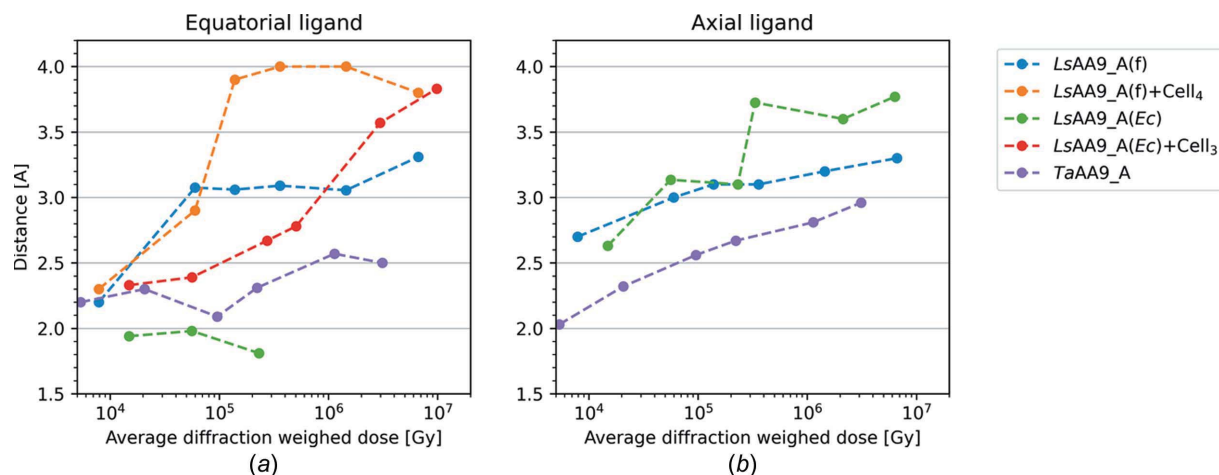
Figure 3
Measured distances as a function of the average diffraction weighted radiation dose. Distances are measured from the Cu atom to either the equatorial ligand or the axial water molecule. In substrate-binding structures, no measurement is taken for the axial water, as it has been displaced by substrate. For *Ls*AA9_A(*Ec*), the density for the equatorial water disappears completely after the third dose structure. All distances are listed in Table S7.

Fig. S11 and Movie S3]. The equatorial water molecule sits at 2.2 Å from the Cu atom in the lowest-dose structure and reaches the longest distance of 2.6 Å at an intermediate dose (1.13×10^6 Gy). Similar to *Ls*AA9_A(*Ec*), the structure of *Ta*AA9_A has a small molecule (modelled as acrylic acid) near the equatorial position [see Figs. 2(*e*) and 2(*f*)], and additionally, a HEPES molecule near the axial position, present from crystallization conditions. It is therefore possible that the presence of these ligands affects the observed distances. However, the axial distance in the EXAFS study may also be affected by some photoreduction even when precautions were taken. *Ta*AA9_A may also be slightly less sensitive to photoreduction than *Ls*AA9_A, as the changes in θ values are slightly smaller for the *Ta*AA9_A transition (Figs. 4 and S6).

For all three substrate-free enzymes used in the photoreduction study, we have obtained a reasonably consistent picture of transition from Cu^{2+} to Cu^+ in diverse AA9 LPMOs under different crystallization conditions. We observe a loss in coordination between Cu and water ligands at higher doses, changing the coordination from an elongated hexacoordinated geometry to a T-shaped geometry with Cu coordinated solely by protein ligands, as discussed previously (Gudmundsson *et al.*, 2014; Vu & Ngo, 2018; Kjaergaard *et al.*, 2014). Previous studies of *Efa*CBM33/*Ef*AA10, using doses in a comparable range to what has been used here (Gudmundsson *et al.*, 2014), showed that at doses higher than 5.94×10^5 Gy the exogenous water ligands were expelled from the initial trigonal bipyramidal geometry. This points towards the T-shaped geometry being essential when accepting the oxygen co-substrate, despite the initial difference in the water-ligand coordination compared to the investigated AA9s. A structure of *Ao*AA13, which has similar Cu geometry to AA9, solved with an X-ray dose of 3.19×10^4 Gy, exhibits a fully reduced Cu site with no visible solvent-facing ligands, and already at the lowest dose (2.57×10^3 Gy) has lost the axial water ligand (Muderspach *et al.*, 2019), suggesting it is more prone to photoreduction than the analyzed AA9s and AA10.

3.3. Serial synchrotron crystallography and room-temperature structures of *Ls*AA9_A

Serial synchrotron crystallography (SSX) experiments are an effective method for reducing radiation damage compared to a conventional MX experiment (de la Mora *et al.*, 2020;
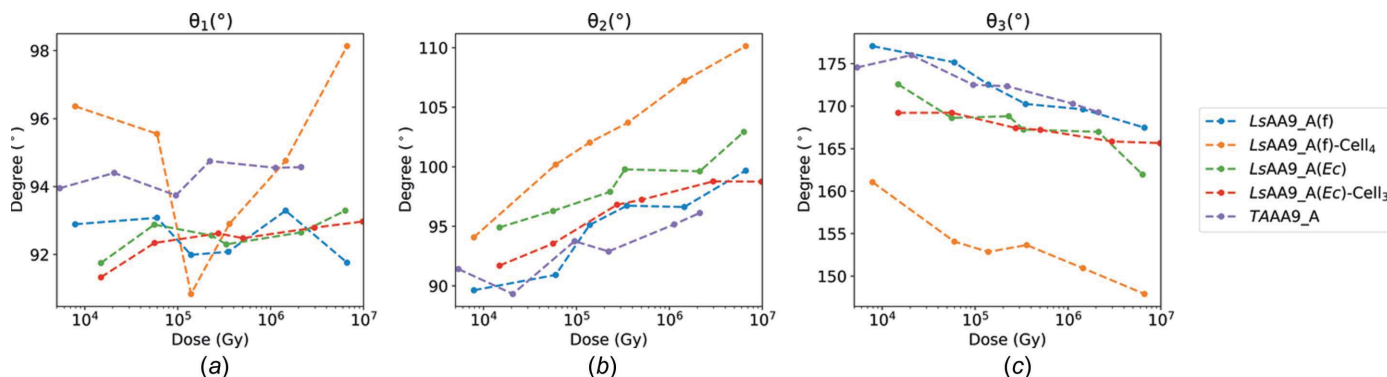

Figure 4
Measured active-site angles θ_1, θ_2 and θ_3 as a function of the average diffraction weighted radiation dose. A consistent observation for all proteins in the photoreduction study is an increase in θ_2 and a decrease in θ_3, while θ_1 is less consistent. All angles are listed in Table S7.

Tobias Tandrup *et al.* · Changes in active-site geometry
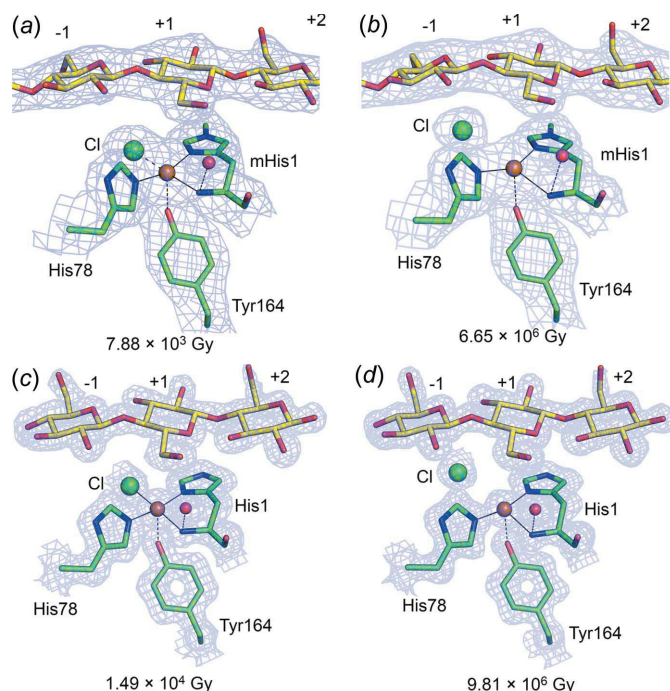
Figure 5
LPMO Cu sites in the oligosaccharide-bound structures of *Ls*AA9_A(f) [(*a*) 7pyd and (*b*) 7pyi] and *Ls*AA9_A(*Ec*) [(*c*) 7pyu and (*d*) 7pz0] at the lowest and highest X-ray doses. For both *Ls*AA9_A(f) and *Ls*AA9_A(*Ec*) at higher X-ray doses, the equatorial Cl⁻ ion (green spheres, present from crystallization conditions) increases its distance relative to the Cu atom. The Tyr164-O to Cu distance is, in all cases, shorter than for the substrate-free structures presented in Fig. 2. Active-site distances are listed in Table 3. $2F_o–F_c$ electron density is shown at a 1.0 contour level as blue mesh.

Ebrahim *et al.*, 2019; Mehrabi *et al.*, 2021) and could allow better control of photoreduction in metalloproteins. Data collected on 13 crystals were scaled together, resulting in the 2.4 Å *Ls*AA9_A(f)-SSX data set. The dose received by the resulting structure (7.02×10^4 Gy) is comparable to the oligosaccharide-free *Ls*AA9_A(f) structure with a dose of 5.99×10^4 Gy, and indeed shows a similar geometry, indicating close to full photoreduction, though with a somewhat sharper θ_1 and wider θ_3 angle. The θ_T angle in the SSX structure is greater than in any of the six *Ls*AA9_A(f) substrate-free structures, or the chemically reduced structures. The axial water molecule was found at 2.9 Å in the *Ls*AA9_A(f)-SSX structure, which agrees with the substrate-free *Ls*AA9_A(f) structure. However, the equatorial water molecule found at 3.9 Å is very indicative of a fully reduced Cu site, despite efforts to limit the dose experienced by each crystal. In part, this could be due to the water in the *Ls*AA9_A(f)-SSX structure having only a single conformation at this position (see Figs. S7 and S12). Perhaps unsurprisingly, SSX does not protect from photoreduction at a similar total dose and it would have been difficult to obtain a lower dose with the applied protocol. The distances observed within the active site are listed in Table 3, and in Tables S7 and S8.

We collected room-temperature data for the *Ls*AA9_A(f) crystals, both from an in-house diffractometer and from a synchrotron, at the lowest possible dose (Fig. S4). Here

*Ls*AA9_A(f) (RT) from the in-house data has distances of 2.2 and 2.8 Å for the equatorial and axial ligands, respectively, which correlate well with a Cu²⁺ state (Vu & Ngo, 2018; Gudmundsson *et al.*, 2014; Frandsen *et al.*, 2016). Perhaps surprisingly, data collected from a synchrotron source at room temperature was similarly able to produce a structure containing a Cu²⁺ site [*Ls*AA9_A(f), RT-sync], based on the Cu–water distances and $\theta_1–\theta_3$ angles (some of the other parameters resemble more a Cu⁺ site). It was in this case possible to achieve a much lower dose than for the corresponding cryogenic temperature structures (1.91×10^3 Gy).

Due to the rapid decay of the diffraction intensity without cryocooling, a fully photoreduced structure could not be determined using this strategy. Curiously, the *Ls*AA9_A(f) (RT) structure contains a Cl⁻ ion in the axial position, which was confirmed by an anomalous signal (see Fig. S4), which in *Ls*AA9_A(f) (RT-sync) appears to be the more regularly observed water ligand.

3.4. Photoreduction of *Ls*AA9_A crystals soaked with oligosaccharides

Data on *Ls*AA9_A crystals soaked in cello-oligosaccharides were collected using the same protocol as for the oligo-saccharide-free crystals. As for the unbound structures, methylation of His1 does not seem to affect photoreduction to any significant extent, nor does it seem to have a structural effect on substrate binding (Frandsen *et al.*, 2016). For both the *Ls*AA9_A(f) and *Ls*AA9_A(*Ec*) oligosaccharide-bound/ unbound structures, the so-called pocket water increases its distance to His1-N with increasing X-ray dose (Figs. 2, 5 S7, S9, S10, S13 and S14). Here also the distance from the equatorial ligand to Cu increases with increasing X-ray dose experienced by the crystal (Tables 3 and S7, and Fig. 5).

At the lowest doses [Figs. 5(*a*) and 5(*c*)], the equatorial solvent-facing ligand, modelled as a Cl⁻ ion, is 2.3 Å from the Cu atom, while in the highest-dose structures, the distance has increased to 3.9 and 3.8 Å for *Ls*AA9_A(f)-Cell₄ and *Ls*AA9_A(*Ec*)-Cell₃, respectively. For comparison, the average distance to the equatorial ligand is 2.1 Å between different QM/MM models in a recent theoretical study (Theibich *et al.*, 2021). In several intermediate X-ray doses of *Ls*AA9_A(f)-Cell₄, the Cl⁻ ion was modelled in a double conformation, with 90% occupancy for the conformation furthest from the Cu atom and 10% occupancy for the conformation closest to the Cu atom, indicating a mixed state between Cu²⁺ and Cu⁺. The distance from the Cl⁻ ion to Cu increases much more rapidly with dose in the *Ls*AA9_A(f)-Cell₄ structures (3.8 Å at 3.60×10^5 Gy) compared to *Ls*AA9_A(*Ec*)-Cell₃ (3.8 Å at 9.81×10^6 Gy) (Figs. S13 and S14, Table S7, and Movies S4 and S5). It is unclear if these differences are due to the differences between the fungally and bacterially expressed enzymes, or if it is a result of the conditions under which the crystals were grown. At any rate, while in the case of the substrate-free *Ls*AA9_A(*Ec*) structure the equatorial position was partially occupied by sulfate (and partially by a water molecule), this does not seem to be the

case for the equatorial ligand at $LsAA9\_A(Ec)$-Cell$_3$, which is most consistent with fully occupied chloride, although this could not be confirmed with an anomalous signal.

As for the transition from Cu^{2+} to Cu^+ in the unbound structures, for the oligosaccharide-bound structures there is a clear increase in the θ_2 angle and a clear decrease in the θ_3 angle (see Fig. 4). Furthermore, all the oligosaccharide-bound structures at any dose have values considerably greater than 0 and greater than those of the corresponding unbound structures for the θ_T angle, i.e. $18.7 \pm 3.3°$ for $LsAA9\_A(f)$ and $8.7 \pm 0.9°$ for $LsAA9\_A(Ec)$ (see Fig. S6). Thus, a significantly greater θ_T angle seems to be a characteristic of oligosaccharide-bound $LsAA9\_A$. To further test this hypothesis, we calculated the average value for all the available structures of $LsAA9\_A$ with bound saccharide ligands, excluding xylooligosaccharides, as they are questionable as true LPMO substrates (Simmons et al., 2017). The average was $11.49 \pm 2.03°$ (PDB entries 5aci, 5acf, 5acj, 5n05, 5nkw, 5nlr, 5nls and 6ydg). As θ_T also increases with dose in the unbound structures, a better comparison may be between low-dose structures for all saccharide-free and saccharide-bound $LsAA9\_A$ structures to date (Table S9), which also shows a greater θ_T value for bound ($12.0 \pm 3.1°$) compared to free ($2.4 \pm 0.9°$).

Several reports have suggested a higher affinity of at least some AA9 LPMOs for cellulosic substrates in their Cu^+ as opposed to their Cu^{2+} form (Kracher et al., 2018; Bertini et al., 2018; Courtade et al., 2016; McEvoy et al., 2021). This has also been demonstrated recently for $LsAA9\_A$ (Brander, Tokin et al., 2021). For both $LsAA9\_A(f)$ and $LsAA9\_A(Ec)$ oligosaccharide-binding structures, there are no considerable structural changes in interactions (e.g. protein-accessible surface or hydrogen bonding) in the Cu^{2+} to Cu^+ transition that can explain the increased affinity. However, since the axial ligand is already lost during reduction, no penalty must be paid for the loss of this interaction in the Cu^+ form.

Furthermore, we have shown that both photoreduction and, to an even larger extent, oligosaccharide binding increases the θ_T angle. Thus, the oligosaccharide-free Cu^+ state is closer in active-site geometry to the oligosaccharide-bound state, which might contribute favourably to binding.

3.5. The active-site tyrosine in oligosaccharide-free and oligosaccharide-bound structures

The role of the Cu-site tyrosine has been proposed to be for protection against auto-oxidation (Paradisi et al., 2019; Singh et al., 2019). Recently, deprotonation of tyrosine as part of the mechanism was investigated through theoretical calculations and spectroscopic measurements to elucidate the formation of the LPMO reaction intermediates cis/trans-$[\text{Tyr-O}^\cdot\text{–Cu}^{2+}\text{–OH}]^+$ (McEvoy et al., 2021). In the unbound state, the formation of Tyr intermediates is associated with a reduction in the Tyr-O to Cu distance of 0.27–0.47 Å (McEvoy et al., 2021). Thus, though a shortening has been reported from a comparison of experimental structures (Frandsen et al., 2016), it was important to confirm it in this more systematic study.

Here, for both $LsAA9\_A$ variants, the distance between Tyr164 and Cu increases by 0.1 Å with increasing radiation dose, while for $TaAA9\_A$, the distance decreases by the same value. These differences may not be significant. However, confirming the previous crystallographic studies (Frandsen et al., 2016; Simmons et al., 2017), the distance from Tyr164-O to Cu is shorter (0.1–0.2 Å) for all the $LsAA9\_A(f)$-Cell$_4$ and $LsAA9\_A(Ec)$-Cell$_3$ structures compared to the corresponding unbound structures (see Fig. 6). This difference may again not seem significant when considering only DPI-based coordinate errors (Kumar et al., 2015; Murshudov et al., 1997). However, there are a number of considerations suggesting that it is significant, at least for the low-dose $LsAA9\_A$ Cu^{2+} structures from this and previous studies (Frandsen et al., 2016), which are listed in Table S9, with the relevant distances
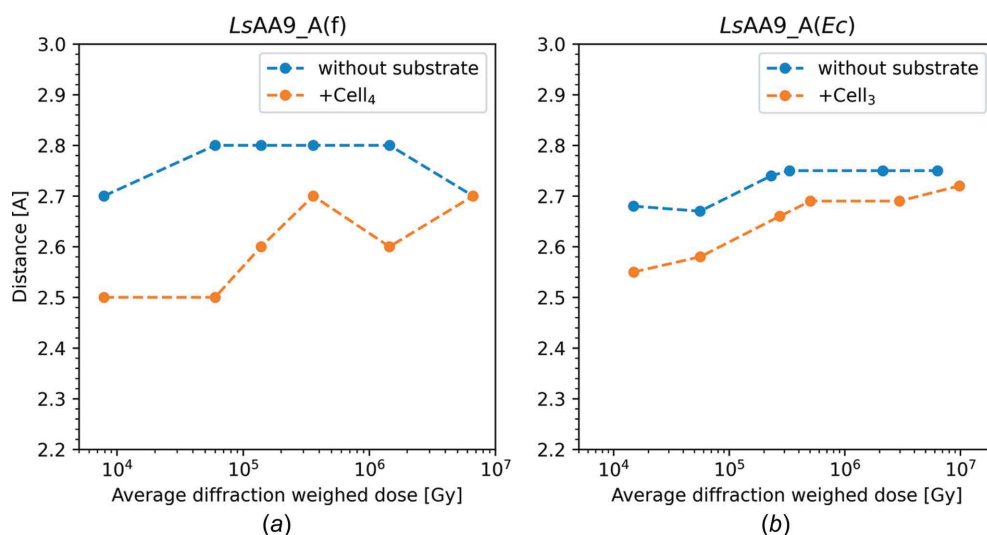

Figure 6
The measured Cu—Tyr-O distance over the Cu^{2+} to Cu^+ transition for $LsAA9\_A(f)$ and $LsAA9\_A(Ec)$. A slight increase in the distance is found over the transition and a more significant reduction in the distances for all doses is found once substrate is bound. This is further presented for the low-dose structures in Movie S6.

and errors presented in Movie S6. First of all, taking each structure as an independent estimate of bond length, the average for the three saccharide-free structures is 2.71 ± 0.031 Å, while for the three saccharide-binding structures, the average is 2.50 ± 0.044 Å, indicating that the real coordinate error may be lower than estimated. Secondly, to investigate the structural changes without influence of the refinement protocol and the presence of the saccharide in the model, we calculated difference maps where only rigid-body refinement was applied to a model of a saccharide-free structure (protein and Cu only, as a single rigid body to maintain a fixed distance) against data for a saccharide-binding structure. Maps calculated for three such pairs show clearly that the data demand the copper–Tyr distance to be shortened (Fig. S15). The reduction in distance between Tyr-O and Cu is also reproduced qualitatively in the QM/MM-optimized structures of LsAA9_A, where the distance was found to decrease by 0.2–0.3 Å upon LsAA9_A binding the substrate (Theibich *et al.*, 2021). While the role of tyrosine remains unclear, the shortening of the Tyr-O to Cu bond has been shown here to be reproducible for LsAA9_A.

4. Conclusion

For metalloproteins, radiation damage in the form of photoreduction is common, and balancing X-ray dose and diffraction intensity is crucial. For LPMOs, photoreduction of the central Cu atom is difficult to avoid in a diffraction experiment, but may reveal details for the first step of the LPMO reaction.

We recommend that researchers wishing to investigate the LPMO Cu^{2+} state plan their experiments to limit the total dose to a few kGy or less if possible and, if necessary, to use helical data collections to reduce the dose. A dose in the MGy range should be used to catch Cu^+ states, or possibly trigger the LPMO reaction. Similarly, we were successful in collecting data on chemically reduced crystals which support a Cu^+ state.

Through our photoreduction study we have monitored various geometrical parameters, which are indicative of the two LPMO Cu states. As the observed changes in distance to protein ligands are small, the best structural diagnostics for the Cu^{2+} to Cu^+ transition in these (and probably other octahedrally coordinated Cu sites) are the θ_3 and θ_T values, where values lower than $170°$ and higher than $3°$, respectively, are strong indicators of a reduced site. Additional indicators may be found in the angles θ_{H-H} and θ_{H1}, which appear lower for a reduced site, and θ_{HN}, which is slightly higher for the Cu^+ state, although the absolute values are inconsistent between the investigated proteins. Non-protein ligands may also be helpful in identifying the Cu state, as we and others have demonstrated, and the final T-shaped geometry of the His-brace seems to be a defining feature of LPMO Cu^+ sites. The exogenous ligands can be affected by the closeness of other molecules present in the active site, which must be considered when interpreting structural data. Thus, when a single-crystal X-ray experiment is performed, these values alone cannot firmly assign a structure as Cu^{2+} or Cu^+.

Upon binding of saccharide substrate, the Cu–Tyr distance in AA9s is found consistently to be shortened, regardless of the Cu state. Based on several independently determined structures and an analysis of difference electron-density maps, we find this small shortening of ~ 0.2 Å significant for the Cu^{2+} structures of LsAA9_A. With previous indications that the active-site Tyr is important for the mechanism, the experimental structures now available at both Cu stages could allow further computational exploration. Correlated to the Cu–Tyr distance changes, while in Cu^{2+} saccharide-free structures the equatorial ligands and Cu are close to being coplanar, saccharide binding induces clear deviation from planarity, as seen in changes of the θ_T angle. As the reduction of Cu also induces geometric changes to the Cu site, including an increase in the θ_T angle, the observed greater affinity of Cu^+ LPMOs for poly- and oligosaccharides may be partly explained by being closer structurally to the oligosaccharide-bound form.

5. Abbreviations

AA: auxiliary activity; ASC: ascorbic acid; ax: Axial; CAZy: Carbohydrate-Active enZymes database; Cell$_3$: cellotriose; Cell$_4$: cellotetraose; EndoH: endoglycosidase-H; Eq: equatorial; LPMO: lytic polysaccharide monooxygenase; LsAA9_A(Ec): LsAA9_A produced in *E. coli*; LsAA9_A(f): LsAA9_A produced in *A. oryzae*; LsAA9_A: family AA9 LPMOs from *Lentinus similis*; MX: macromolecular crystallography; QM/MM: quantum mechanics/molecular mechanics; RT: room temperature; SSX: serial synchrotron crystallography; TaAA9_A: family AA9 LPMOs from *Thermoascus aurantiacus*.

supported by the Danish Ministry of Higher Education and Science through the instrument centre DANSCATT and the Seventh Framework Programme of the European Community under BioStruct-X (grant agreement No. 283570). TT, SJM, SB and LLL are members of ISBUC (Integrative Structural Biology at the University of Copenhagen, www.isbuc.ku.dk). The author contributions are as follows: LLL conceived the study and, together with TT, planned the study and experiments. TT crystallized the protein samples *Ls*AA9_A(f), *Ls*AA9_A(SSX), *Ls*AA9_A(RT), *Ls*AA9_A (RT-synchrotron) and *Ta*AA9_A, and optimized the parameters for the crystallographic data-collection strategies. TT collected and analyzed the crystallographic data, solved the crystal structures and made the structural figures and tables. SJM and SB crystallized protein sample *Ls*AA9_A(*Ec*), collected and analyzed the crystallographic data, assisted by TT, and made the supplementary figures. TT and SB collected the data on chemically reduced protein crystals, solved the crystal structures and made the figures and tables. GS and TT collected and analyzed the crystallographic data for *Ls*AA9_A-SSX. TT and FM collected the crystallographic data for *Ls*AA9_A-RT. SB measured and analyzed the geometric parameters and made the structural tables. CHR and MHHN expressed the *Ls*AA9_A(*Ec*) samples. JØI purified and prepared the *Ls*AA9_A(*Ec*) sample for crystallization. LLL, MN, FM and KSJ supervised the experimental work. LLL and TT wrote the manuscript, with contributions from SB and SJM. All authors contributed to the editing of the manuscript and approved the final version. The authors declare no conflict of interest.

References

Almeida, K. J. de, Murugan, N. A., Rinkevicius, Z., Hugosson, H. W., Vahtras, O., Ågren, H. & Cesar, A. (2009). *Phys. Chem. Chem. Phys.* **11**, 508–519.
Antonyuk, S. V. & Hough, M. A. (2011). *Biochim. Biophys. Acta*, **1814**, 778–784.
Banerjee, S., Muderspach, S. J., Tandrup, T., Frandsen, K. E. H., Singh, R. K., Ipsen, J. Ø., Hernández-Rollán, C., Nørholm, M. H. H., Bjerrum, M. J., Johansen, K. S. & Lo Leggio, L. (2022). *Biomolecules*, **12**, 194.
Beeson, W. T., Vu, V. V., Span, E. A., Phillips, C. M. & Marletta, M. A. (2015). *Annu. Rev. Biochem.* **84**, 923–946.
Bertini, L., Breglia, R., Lambrughi, M., Fantucci, P., De Gioia, L., Borsari, M., Sola, M., Bortolotti, C. A. & Bruschi, M. (2018). *Inorg. Chem.* **57**, 86–97.
Bissaro, B., Røhr, Å. K., Müller, G., Chylenski, P., Skaugen, M., Forsberg, Z., Horn, S. J., Vaaje-Kolstad, G. & Eijsink, V. G. H. (2017). *Nat. Chem. Biol.* **13**, 1123–1128.

Bissaro, B., Streit, B., Isaksen, I., Eijsink, V. G. H., Beckham, G. T., DuBois, J. L. & Røhr, Å. K. (2020). *Proc. Natl Acad. Sci.* **117**, 1504–1513.
Bourgeois, D. (2017). *Int. J. Mol. Sci.* **18**, 1187.
Bourgeois, D. & Royant, A. (2005). *Curr. Opin. Struct. Biol.* **15**, 538–547.
Bourgeois, D. & Weik, M. (2009). *Crystallogr. Rev.* **15**, 87–118.
Bowman, S. E. J., Bridwell-Rabb, J. & Drennan, C. L. (2016). *Acc. Chem. Res.* **49**, 695–702.
Brander, S., Horvath, I., Ipsen, J. Ø., Peciulyte, A., Olsson, L., Hernández-Rollán, C., Nørholm, M. H. H., Mossin, S., Lo Leggio, L., Probst, C., Thiele, D. J. & Johansen, K. S. (2020). *Sci. Rep.* **10**, 16369.
Brander, S., Lausten, S., Ipsen, J. Ø., Falkenberg, K. B., Bertelsen, A. B., Nørholm, M. H. H., Østergaard, L. H. & Johansen, K. S. (2021). *Biotechnol. Biofuels*, **14**, 51.
Brander, S., Tokin, R., Ipsen, J. Ø., Jensen, P. E., Hernández-Rollán, C., Nørholm, M. H. H., Lo Leggio, L., Dupree, P. & Johansen, K. S. (2021). *ACS Catal.* **11**, 13848–13859.
Brenelli, L., Squina, F. M., Felby, C. & Cannella, D. (2018). *Biotechnol. Biofuels*, **11**, 10.
Burkhardt, A., Pakendorf, T., Reime, B., Meyer, J., Fischer, P., Stübe, N., Panneerselvam, S., Lorbeer, O., Stachnik, K., Warmer, M., Rödig, P., Göries, D. & Meents, A. (2016). *Eur. Phys. J. Plus*, **131**, 56.
Cao, L., Caldararu, O., Rosenzweig, A. C. & Ryde, U. (2018). *Angew. Chem. Int. Ed.* **57**, 162–166.
Chen, A. Y., Adamek, R. N., Dick, B. L., Credille, C. V., Morrison, C. N. & Cohen, S. M. (2019). *Chem. Rev.* **119**, 1323–1455.
Cock, P. J. A., Antao, T., Chang, J. T., Chapman, B. A., Cox, C. J., Dalke, A., Friedberg, I., Hamelryck, T., Kauff, F., Wilczynski, B. & de Hoon, M. J. L. (2009). *Bioinformatics*, **25**, 1422–1423.
Corbett, M. C., Latimer, M. J., Poulos, T. L., Sevrioukova, I. F., Hodgson, K. O. & Hedman, B. (2007). *Acta Cryst.* **D63**, 951–960.
Courtade, G., Ciano, L., Paradisi, A., Lindley, P. J., Forsberg, Z., Sørlie, M., Wimmer, R., Davies, G. J., Eijsink, V. G. H., Walton, P. H. & Aachmann, F. L. (2020). *Proc. Natl Acad. Sci. USA*, **117**, 19178–19189.
Courtade, G., Wimmer, R., Røhr, K., Preims, M., Felice, A. K. G., Dimarogona, M., Vaaje-Kolstad, G., Sørlie, M., Sandgren, M., Ludwig, R., Eijsink, V. G. H. & Aachmann, F. L. (2016). *Proc. Natl Acad. Sci. USA*, **113**, 5922–5927.
Ebrahim, A., Moreno-Chicano, T., Appleby, M. V., Chaplin, A. K., Beale, J. H., Sherrell, D. A., Duyvesteyn, H. M. E., Owada, S., Tono, K., Sugimoto, H., Strange, R. W., Worrall, J. A. R., Axford, D., Owen, R. L. & Hough, M. A. (2019). *IUCrJ*, **6**, 543–551.
Eijsink, V. G. H., Petrovic, D., Forsberg, Z., Mekasha, S., Røhr, Å. K., Várnai, A., Bissaro, B. & Vaaje-Kolstad, G. (2019). *Biotechnol. Biofuels*, **12**, 58.
Emsley, P. & Cowtan, K. (2004). *Acta Cryst.* **D60**, 2126–2132.
Evans, P. (2006). *Acta Cryst.* **D62**, 72–82.
Evans, P. R. & Murshudov, G. N. (2013). *Acta Cryst.* **D69**, 1204–1214.
Festa, R. A. & Thiele, D. J. (2011). *Curr. Biol.* **21**, R877–R883.
Filandr, F., Man, P., Halada, P., Chang, H., Ludwig, R. & Kracher, D. (2020). *Biotechnol. Biofuels*, **13**, 37.
Frandsen, K. E. H. & Lo Leggio, L. (2016). *IUCrJ*, **3**, 448–467.
Frandsen, K. E. H., Poulsen, J. N., Tandrup, T. & Lo Leggio, L. (2017). *Carbohydr. Res.* **448**, 187–190.
Frandsen, K. E. H., Simmons, T. J., Dupree, P., Poulsen, J. N., Hemsworth, G. R., Ciano, L., Johnston, E. M., Tovborg, M., Johansen, K. S., von Freiesleben, P., Marmuse, L., Fort, S., Cottaz, S., Driguez, H., Henrissat, B., Lenfant, N., Tuna, F., Baldansuren, A., Davies, G. J., Lo Leggio, L. & Walton, P. H. (2016). *Nat. Chem. Biol.* **12**, 298–303.
Frankaer, C. G., Mossin, S., Ståhl, K. & Harris, P. (2014). *Acta Cryst.* **D70**, 110–122.
Frommhagen, M., Mutte, S. K., Westphal, A. H., Koetsier, M. J., Hinz, S. W. A. A., Visser, J., Vincken, J.-P. P., Weijers, D., van Berkel, W. J.

H. H., Gruppen, H. & Kabel, M. A. (2017). *Biotechnol. Biofuels*, **10**, 121.

Garcia-Santamarina, S., Probst, C., Festa, R. A., Ding, C., Smith, A. D., Conklin, S. E., Brander, S., Kinch, L. N., Grishin, N. V., Franz, K. J., Riggs-Gelasco, P., Lo Leggio, L., Johansen, K. S. & Thiele, D. J. (2020). *Nat. Chem. Biol.* **16**, 337–344.

Gudmundsson, M., Kim, S., Wu, M., Ishida, T., Momeni, M. H., Vaaje-Kolstad, G., Lundberg, D., Royant, A., Ståhlberg, J., Eijsink, V. G. H., Beckham, G. T. & Sandgren, M. (2014). *J. Biol. Chem.* **289**, 18782–18792.

Handing, K. B., Niedzialkowska, E., Shabalin, I. G., Kuhn, M. L., Zheng, H. & Minor, W. (2018). *Nat. Protoc.* **13**, 1062–1090.

Hangasky, J. A., Iavarone, A. T. & Marletta, M. A. (2018). *Proc. Natl Acad. Sci. USA*, **115**, 4915–4920.

Hangasky, J. A. & Marletta, M. A. (2018). *Biochemistry*, **57**, 3191–3199.

Harris, P. V., Welner, D., McFarland, K. C., Re, E., Navarro Poulsen, J.-C., Brown, K., Salbo, R., Ding, H., Vlasenko, E., Merino, S., Xu, F., Cherry, J., Larsen, S. & Lo Leggio, L. (2010). *Biochemistry*, **49**, 3305–3316.

Hedegård, E. D. & Ryde, U. (2017). *J. Biol. Inorg. Chem.* **22**, 1029–1037.

Hedegård, E. D. & Ryde, U. (2018). *Chem. Sci.* **9**, 3866–3880.

Helliwell, J. R. (1984). *Rep. Prog. Phys.* **47**, 1403–1497.

Hemsworth, G. R., Davies, G. J. & Walton, P. H. (2013). *Curr. Opin. Struct. Biol.* **23**, 660–668.

Hernández-Rollán, C., Falkenberg, K. B., Rennig, M., Bertelsen, A. B., Ipsen, J. Ø., Brander, S., Daley, D. O., Johansen, K. S. & Nørholm, M. H. H. (2021). *ACS Synth. Biol.* **10**, 897–906.

Hoppert, M. (2011). *Encyclopedia of Geobiology*, edited by J. Reitner & V. Thiel, pp. 558–563. Dordrecht: Springer.

Ipsen, J. Ø., Hallas-Møller, M., Brander, S., Lo Leggio, L. & Johansen, K. S. (2021). *Biochem. Soc. Trans.* **49**, 531–540.

Jahn, H. A. & Teller, E. (1937). *Proc. R. Soc. London. Ser. A Math. Phys. Sci.* **161**, 220–235.

Johansen, K. S. (2016). *Biochem. Soc. Trans.* **44**, 143–149.

Kabsch, W. (2010). *Acta Cryst.* D**66**, 125–132.

Kim, S., Ståhlberg, J., Sandgren, M., Paton, R. S. & Beckham, G. T. (2014). *Proc. Natl Acad. Sci. USA*, **111**, 149–154.

Kjaergaard, C. H., Qayyum, M. F., Wong, S. D., Xu, F., Hemsworth, G. R., Walton, D. J., Young, O., Davies, G. J., Walton, P. H., Johansen, K. S., Hodgson, K. O., Hedman, B. & Solomon, E. I. (2014). *Proc. Natl Acad. Sci. USA*, **111**, 8797–8802.

Kracher, D., Andlar, M., Furtmüller, P. G. & Ludwig, R. (2018). *J. Biol. Chem.* **293**, 1676–1687.

Kracher, D., Scheiblbrandner, S., Felice, A. K. G., Breslmayr, E., Preims, M., Ludwicka, K., Haltrich, D., Eijsink, V. G. H. & Ludwig, R. (2016). *Science*, **352**, 1098–1101.

Kumar, K. S. D., Gurusaran, M., Satheesh, S. N., Radha, P., Pavithra, S., Thulaa Tharshan, K. P. S., Helliwell, J. R. & Sekar, K. (2015). *J. Appl. Cryst.* **48**, 939–942.

Labourel, A., Frandsen, K. E. H., Zhang, F., Brouilly, N., Grisel, S., Haon, M., Ciano, L., Ropartz, D., Fanuel, M., Martin, F., Navarro, D., Rosso, M., Tandrup, T., Bissaro, B., Johansen, K. S., Zerva, A., Walton, P. H., Henrissat, B., Lo Leggio, L. & Berrin, J. G. (2020). *Nat. Chem. Biol.* **16**, 345–350.

Lo Leggio, L., Simmons, T. J., Poulsen, J. N., Frandsen, K. E. H., Hemsworth, G. R., Stringer, M. A., von Freiesleben, P., Tovborg, M., Johansen, K. S., De Maria, L., Harris, P. V., Soong, C.-L., Dupree, P., Tryfona, T., Lenfant, N., Henrissat, B., Davies, G. J. & Walton, P. H. (2015). *Nat. Commun.* **6**, 5961.

Lombard, V., Golaconda Ramulu, H., Drula, E., Coutinho, P. M. & Henrissat, B. (2014). *Nucleic Acids Res.* **42**, D490–D495.

McEvoy, A., Creutzberg, J., Singh, R. K., Bjerrum, M. J. & Hedegård, E. D. (2021). *Chem. Sci.* **12**, 352–362.

Mehrabi, P., Bücker, R., Bourenkov, G., Ginn, H. M., von Stetten, D., Müller-Werkmeister, H. M., Kuo, A., Morizumi, T., Eger, B. T., Ou, W.-L., Oghbaey, S., Sarracini, A., Besaw, J. E., Paré-Labrosse, O.,

Meier, S., Schikora, H., Tellkamp, F., Marx, A., Sherrell, D. A., Axford, D., Owen, R. L., Ernst, O. P., Pai, E. F., Schulz, E. C. & Miller, R. J. D. (2021). *Sci. Adv.* **7**, eabf1380.

Mora, E. de la, Coquelle, N., Bury, C. S., Rosenthal, M., Holton, J. M., Carmichael, I., Garman, E. F., Burghammer, M., Colletier, J.-P. & Weik, M. (2020). *Proc. Natl Acad. Sci.* **117**, 4142–4151.

Muderspach, S. J., Tandrup, T., Frandsen, K. E. H., Santoni, G., Poulsen, J. N. & Lo Leggio, L. (2019). *Amylase*, **3**, 41–54.

Müller, G., Chylenski, P., Bissaro, B., Eijsink, V. G. H. & Horn, S. J. (2018). *Biotechnol. Biofuels*, **11**, 209.

Müller, G., Várnai, A., Johansen, K. S., Eijsink, V. G. H. & Horn, S. J. (2015). *Biotechnol. Biofuels*, **8**, 187.

Murshudov, G. N., Vagin, A. A. & Dodson, E. J. (1997). *Acta Cryst.* D**53**, 240–255.

Paradisi, A., Johnston, E. M., Tovborg, M., Nicoll, C. R., Ciano, L., Dowle, A., McMaster, J., Hancock, Y., Davies, G. J. & Walton, P. H. (2019). *J. Am. Chem. Soc.* **141**, 18585–18599.

Peciulyte, A., Samuelsson, L., Olsson, L., McFarland, K. C., Frickmann, J., Østergård, L., Halvorsen, R., Scott, B. R. & Johansen, K. S. (2018). *Biotechnol. Biofuels*, **11**, 165.

Persson, I. (2010). *Pure Appl. Chem.* **82**, 1901–1917.

Quinlan, R. J., Sweeney, M. D., Lo Leggio, L., Otten, H., Poulsen, J. N., Johansen, K. S., Krogh, K. B. R. M., Jørgensen, C. I., Tovborg, M., Anthonsen, A., Tryfona, T., Walter, C. P., Dupree, P., Xu, F., Davies, G. J. & Walton, P. H. (2011). *Proc. Natl Acad. Sci. USA*, **108**, 15079–15084.

Sabbadin, F., Urresti, S., Henrissat, B., Avrova, A. O., Welsh, L. R. J., Lindley, P. J., Csukai, M., Squires, J. N., Walton, P. H., Davies, G. J., Bruce, N. C., Whisson, S. C. & McQueen-Mason, S. J. (2021). *Science*, **373**, 774–779.

Sanctis, D. de, Beteva, A., Caserotto, H., Dobias, F., Gabadinho, J., Giraud, T., Gobbo, A., Guijarro, M., Lentini, M., Lavault, B., Mairs, T., McSweeney, S., Petitdemange, S., Rey-Bakaikoa, V., Surr, J., Theveneau, P., Leonard, G. A. & Mueller-Dieckmann, C. (2012). *J. Synchrotron Rad.* **19**, 455–461.

Santoni, G., Zander, U., Mueller-Dieckmann, C., Leonard, G. & Popov, A. (2017). *J. Appl. Cryst.* **50**, 1844–1851.

Schotte, F., Cho, H. S., Kaila, V. R. I., Kamikubo, H., Dashdorj, N., Henry, E. R., Graber, T. J., Henning, R., Wulff, M., Hummer, G., Kataoka, M. & Anfinrud, P. A. (2012). *Proc. Natl Acad. Sci. USA*, **109**, 19256–19261.

Schröder, G. C. & Meilleur, F. (2021). *Acta Cryst.* D**77**, 1251–1269.

Simmons, T. J., Frandsen, K. E. H., Ciano, L., Tryfona, T., Lenfant, N., Poulsen, J. C., Wilson, L. F. L., Tandrup, T., Tovborg, M., Schnorr, K., Johansen, K. S., Henrissat, B., Walton, P. H., Lo Leggio, L. & Dupree, P. (2017). *Nat. Commun.* **8**, 1064.

Singh, R. K., Blossom, B. M., Russo, D. A., Singh, R., Weihe, H., Andersen, N. H., Tiwari, M. K., Jensen, P. E., Felby, C. & Bjerrum, M. J. (2020). *Chem. Eur. J.* **26**, 454–463.

Solomon, E. I., Heppner, D. E., Johnston, E. M., Ginsbach, J. W., Cirera, J., Qayyum, M., Kieber-Emmons, M. T., Kjaergaard, C. H., Hadt, R. G. & Tian, L. (2014). *Chem. Rev.* **114**, 3659–3853.

Tandrup, T., Frandsen, K. E. H., Johansen, K. S., Berrin, J. & Lo Leggio, L. (2018). *Biochem. Soc. Trans.* **46**, 1431–1447.

Tandrup, T., Tryfona, T., Frandsen, K. E. H., Johansen, K. S., Dupree, P. & Lo Leggio, L. (2020). *Biochemistry*, **59**, 3347–3358.

Theibich, Y. A., Sauer, S. P. A., Lo Leggio, L. & Hedegård, E. D. (2021). *Comput. Struct. Biotechnol. J.* **19**, 555–567.

Udagedara, S. R., Wijekoon, C. J. K., Xiao, Z., Wedd, A. G. & Maher, M. J. (2019). *J. Inorg. Biochem.* **195**, 194–200.

Ursby, T., Åhnberg, K., Appio, R., Aurelius, O., Barczyk, A., Bartalesi, A., Bjelčić, M., Bolmsten, F., Cerenius, Y., Doak, R. B., Eguiraun, M., Eriksson, T., Friel, R. J., Gorgisyan, I., Gross, A., Haghighat, V., Hennies, F., Jagudin, E., Norsk Jensen, B., Jeppsson, T., Kloos, M., Lidon-Simon, J., de Lima, G. M. A., Lizatovic, R., Lundin, M., Milan-Otero, A., Milas, M., Nan, J., Nardella, A., Rosborg, A., Shilova, A., Shoeman, R. L., Siewert, F., Sondhauss, P.,

Talibov, V. O., Tarawneh, H., Thånell, J., Thunnissen, M., Unge, J., Ward, C., Gonzalez, A. & Mueller, U. (2020). *J. Synchrotron Rad.* **27**, 1415–1429.

Vaaje-Kolstad, G., Westereng, B., Horn, S. J., Liu, Z., Zhai, H., Sørlie, M. & Eijsink, V. G. H. (2010). *Science*, **330**, 219–222.

Vagin, A. & Teplyakov, A. (1997). *J. Appl. Cryst.* **30**, 1022–1025.

Vaguine, A. A., Richelle, J. & Wodak, S. J. (1999). *Acta Cryst.* D**55**, 191–205.

Várnai, A., Umezawa, K., Yoshida, M. & Eijsink, V. G. H. (2018). *Appl. Environ. Microbiol.* **84**, e00156-18.

Vu, V. V. & Ngo, S. T. (2018). *Coord. Chem. Rev.* **368**, 134–157.

Waldron, K. J., Rutherford, J. C., Ford, D. & Robinson, N. J. (2009). *Nature*, **460**, 823–830.

Wang, B., Wang, Z., Davies, G. J., Walton, P. H. & Rovira, C. (2020). *ACS Catal.* **10**, 12760–12769.

Winn, M. D., Ballard, C. C., Cowtan, K. D., Dodson, E. J., Emsley, P., Evans, P. R., Keegan, R. M., Krissinel, E. B., Leslie, A. G. W., McCoy, A., McNicholas, S. J., Murshudov, G. N., Pannu, N. S., Potterton, E. A., Powell, H. R., Read, R. J., Vagin, A. & Wilson, K. S. (2011). *Acta Cryst.* D**67**, 235–242.

Yano, J., Kern, J., Irrgang, K.-D., Latimer, M. J., Bergmann, U., Glatzel, P., Pushkar, Y., Biesiadka, J., Loll, B., Sauer, K., Messinger, J., Zouni, A. & Yachandra, V. K. (2005). *Proc. Natl Acad. Sci.* **102**, 12047–12052.

Zander, U., Bourenkov, G., Popov, A. N., de Sanctis, D., Svensson, O., McCarthy, A. A., Round, E., Gordeliy, V., Mueller-Dieckmann, C. & Leonard, G. A. (2015). *Acta Cryst.* D**71**, 2328–2343.

Zeldin, O. B., Gerstel, M. & Garman, E. F. (2013). *J. Appl. Cryst.* **46**, 1225–1230.

Zerva, A., Pentari, C., Grisel, S., Berrin, J.-G. & Topakas, E. (2020). *Biotechnol. Biofuels*, **13**, 142.